Stony Brook University

Synchrotron X-ray Characterization of Structural Defects in III-Nitride Wide Bandgap Semiconductors

A Thesis Presented

by

Shuang Wu

to

The Graduate School

in Partial Fulfillment of the

Requirements

for the Degree of

Master of Science

in

Materials Science and Chemical Engineering

Stony Brook University

May 2017

Stony Brook University

The Graduate School

Shuang Wu

We, the thesis committee for the above candidate for the

Master of Science degree, hereby recommend

acceptance of this thesis.

Michael Dudley – Thesis Advisor
Professor, Department of Materials Science and Chemical Engineering

Balaji Raghothamachar – Second Reader
Research Professor, Department of Materials Science and Chemical Engineering

T.A. Venkatesh – Third Reader
Associate Professor, Department of Materials Science and Chemical Engineering

This thesis is accepted by the Graduate School

Charles Taber
Dean of the Graduate School

Abstract of the Thesis

Synchrotron X-ray Characterization of Structural Defects in III-Nitride Wide Bandgap Semiconductors

by

Shuang Wu

Master of Science

in

Materials Science and Chemical Engineering

Stony Brook University

2017

III-nitrides have long been viewed as promising semiconductor materials for their wide-band gap and high efficiency for emitting light. They have been widely used in electronic and optoelectronic devices, even in the extreme environments such as high frequencies, high voltages and high temperatures. Despite their favorable properties, their performance is strongly affected by factors; such as the growth method employed and consequently the defect types generated and their quantity. In this thesis, the wide bandgap III-nitrides, aluminum nitride (AlN) and gallium nitride (GaN) will be discussed in the aspect of structure, properties and defects characterization. The density of defects, particularly basal plane dislocations and threading edge and screw dislocations, will be measured across multiple wafers and analyzed in order to gain insights into origins of these defects with respect to the growth process employed. Other defects like low angle grain boundaries and prismatic slip bands are also observed and analyzed. In this study, synchrotron white beam and monochromatic X-ray topography are the main techniques employed to characterize samples, with Nomarski optical microscopy used in a complementary manner.

For physical vapor transport (PVT) grown AlN wafers, the distribution of basal plane dislocations and threading dislocations imaged and analyzed synchrotron X-ray topography reveals a wide range of densities from as low as $1.7\times10^{2}cm^{-2}$ to greater than $10^{6}cm^{-2}$, the resolution limit for X-ray topography techniques. For basal plane dislocations (BPDs), the average density is $1.6747\times10^{4}\ cm^{-2}$. As for threading dislocations (TDs), both screw and edge, the average dislocation density is about $1.5515\times10^{4}\ cm^{-2}$ ranging from a low of $3.00\times10^{2}cm^{-2}$ to

a high of $4.477\times10^{4}cm^{-2}$. These differences among the wafers, is clearly attributable to variations in growth conditions.

For hydride vapor phase epitaxy (HVPE) grown GaN wafers on ammonothermal GaN substrates, the threading dislocations and basal plane dislocations in c-plane wafers are observed clearly by synchrotron X-ray topography. The dislocation density of BPDs is relatively low and they are distributed non-uniformly. The average BPD density for c-plane samples is about $1.509\times10^{4}cm^{-2}$ and for TEDs, the dislocation density is of the order of a few $10^{3}cm^{-2}$, and TSD density is about $10^{2}cm^{-2}$. Axial wafers with a-plane and m-plane orientations have been characterized and reveal the evolution of defects due to variations in growth conditions in the c-axis growth directions.

Table of Contents

List of Figures

List of Tables

List of Abbreviations

AlN	Aluminum Nitride
GaN	Gallium Nitride
InN	Indium Nitride
UV	Ultraviolet
LDs	Laser Diodes
LEDs	Light-Emitting Diodes
HCP	Hexagonal Close-Packed
BPD	Basal Plane Dislocation
TD	Threading Dislocation
TED	Threading Edge Dislocation
TSD	Threading Screw Dislocation
TMD	Threading Mixed Dislocation
MOVPE	Metal Organic Vapor Phase Epitaxy
PVT	Physical Vapor Transport
CVD	Chemical Vapour Deposition
HVPE	Hydride Vapour Phase Epitaxy
MOVPE	Metallo Organic Vapour Phase Epitaxy
MBE	Molecular Beam Epitaxy
SR-XRT	Synchrotron Radiation X-ray Topography
LAGB	Low Angle Grain Boundaries

Acknowledgments

After an intensive period of study, I would like to give my sincere appreciation to all the people who have supported and helped me. From my aspect, they not only guide me in the scientific area, but also personally.

I would first like to thank my advisor, Prof. Michael Dudley, for all of the opportunities I was given to conduct my research. What's more, I appreciate his guidance of my research and future.

Second I would particularly like to single out Prof. Balaji Raghothamachar for his excellent cooperation and great patience during my research. His suggestions and encouragement both on the research and thesis help me a lot.

And I would like to thank Prof. T.A. Venkatesh for reviewing my thesis.

I would also like to thank my parents who support me to finish my Masters degree. They are always there for me and whatever happened, they will give me guidance and believe me I can get myself out of the hard situation. It's the family that makes me have courage to create possibility.

In addition, I would like to thank my colleagues, Yu Yang and Jianqiu Guo, for all the support during my research.

Synchrotron X-ray Characterization of Structural Defects in III-Nitride Wide Bandgap Semiconductors

Chapter 1.Introduction

The group III nitrides (AlN, GaN and InN) represent an important trio of semiconductors because of their direct band gaps which span the range 1.95-6.2 eV, including the whole of the visible region and extending well out into the ultraviolet (UV) range [1]. In which, the energy gaps can range from InN (1.9eV), then GaN (3.4eV), and AlN (6.2eV). Two important applications have been apparent for some time, those of short wavelength laser diodes (LDs) for optical disk readout and high-efficiency light-emitting diodes (LEDs) for full color display [1]. With the unique property, group III-nitride-based ultraviolet (UV) light-emitting diodes (LEDs) are being widely applied in optical devices. InAlGaN materials are ideally suited for the realization of UV LEDs since they are applicable throughout the entire UV-A (400–320 nm) and UV-B (320–280 nm) ranges and even access a large segment of the UV-C (280–200 nm) spectral range [2]. Group III-nitrides have also found applications in other electronic devices. For example, advanced GaN/AlGaN high-power microwave transistors are now commercially available [3].

1.1 Structure

The III-group nitrides have long been viewed as promising semiconductor materials for their application in the blue and ultraviolet wavelengths optical devices, as well as high power and high temperature electronic devices [4]. Aluminum nitride (AlN) and gallium nitride (GaN) will be discussed in this thesis, in the aspect of structure, properties, defects and characterization. From recent research, AlN or GaN can mainly present two allotropic forms: the first one is wurtzite type at low pressure. As shown in Figure 1.1 WZ and Figure 1.2 [5], the wurtzite structure is two interpenetrated hexagonal close-packed (HCP) sub-lattices of aluminum/gallium and nitrogen displaced from each other along [0001]. The second one is zinc blende structure, as represented in Figure 1.1 ZB. It is found that the ground state energy of the zinc blende phase is higher than that of the wurtzite phase, which demonstrates that the zinc blende phase is a metastable phase. As shown in Figure 1.3, another type is an allotrope with the rock salt structure. Moreover, the wurtzite and zinc blende phases transform into the rock salt phase at 17 and 15 GPa, respectively [6].

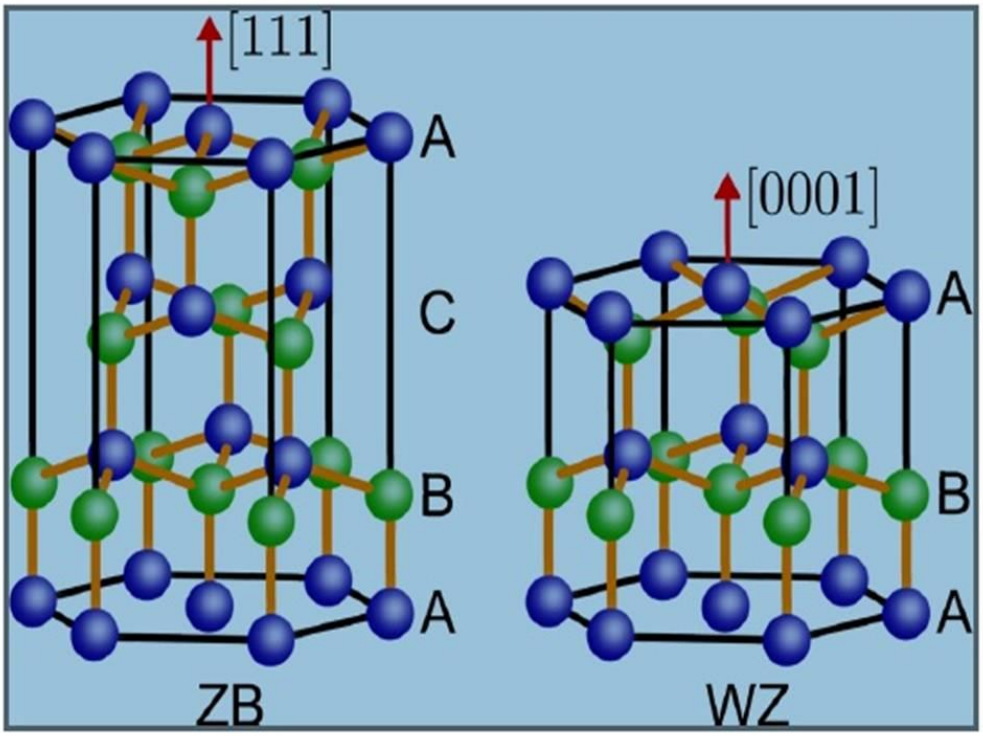

Figure 1.1 Hexagonal close packed (or WZ) crystal structure and zinc-blende (ZB) structure of AlN/GaN.

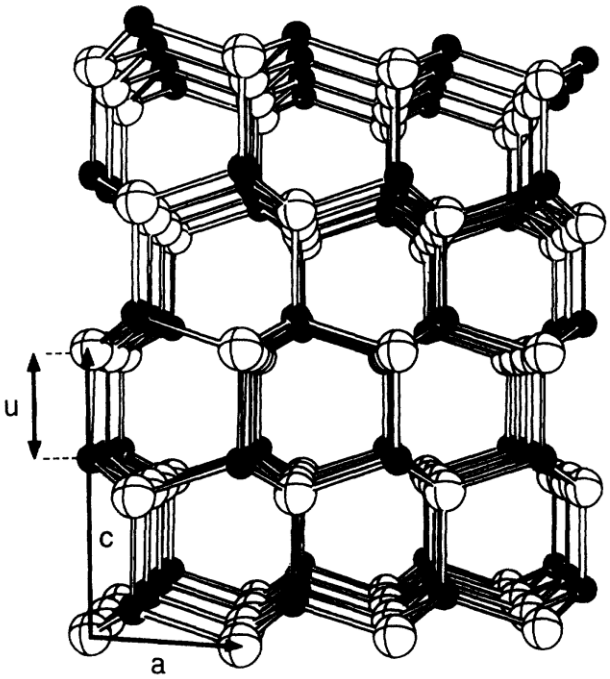

Figure 1.2 Wurtzite structure of AlN/GaN. White represents N atom, black for Al/Ga atom.

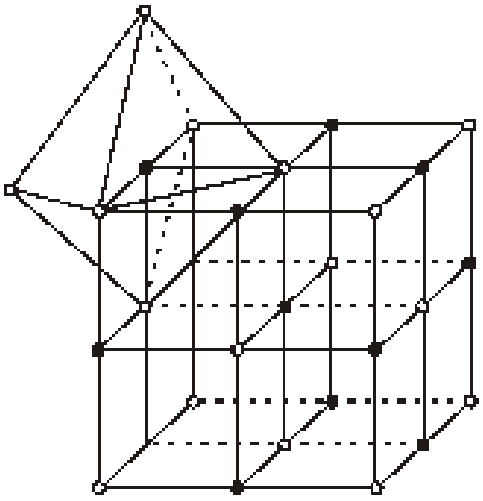

Figure 1.3 Rock salt structure of AlN/GaN.

1.2 Defects Study

From early research, it is reported that the remarkably high TD densities in the III-nitrides lead to speculation that TDs were benign in the nitrides or perhaps even beneficial for the optoelectronic properties [7]. However, with the development of technique and more and more interest in III group semiconductors, it is well known that structural defects such as dislocations, low-angle grain boundaries, inclusions, growth sector boundaries, and twins present in a substrate and intersecting the growth interface will replicate into epitaxial layers and adversely affect the performance and lifetime of devices fabricated on them [8]. As a result, a good understanding about how these defects can affect the performance of the devices is of great significance.

For the structure defects in crystal, it can be mainly characterized by four groups: point defects, line defects, planer defects and volume defects.

1.2.1 Point Defects

Point defects are usually vacancies, interstitials or impurity atoms in the crystal. There are two kinds of point defects in a crystal. The first one is the occupancy of a lattice sites by impurity atoms/ions or voids; the second one is extra atoms/ions not in regular lattice positions. These defects can modify the properties of a sample from that of a perfect crystal. Furthermore, imperfection due to vacancy is also called a Schottky defect. It is created by transferring an atom/ion from the original site to the surface of the sample. At higher temperatures, the number of vacant sites will increase consequently. In the other case, if the atom is transferred to an interstitial position instead of surface, the defect is known as Frenkel defect. This Frenkel defects can explain the mechanism of electric conductivity in ionic salts. In these ionic salts, it is the Frenkel defects that make the electric conductivity rather than electrons. In this thesis, point defects will not be addressed further.

1.2.2 Line Defects

Line defects, are mainly dislocations, such as basal plane dislocation (BPD) and threading dislocation (TD). For the basal plane dislocation (BPD), which is a kind of deformation-induced dislocation, which lie on the basal plane (0001), and the Burger's vector is

1/3[1120].And for the other one, threading dislocations (TDs), which are formed during the growth of the crystal. This kind of dislocations always runs along the normal of the growth plane, in this case, the dislocation line is more or less parallel to the growth direction. Depending on Burger's vector, threading dislocations can be classified as 3 kinds, Threading Edge Dislocation (TED), Threading Screw Dislocations (TSD), and Threading Mixed Dislocation (TMD). For TED, the dislocation line is perpendicular to the Burger's vector, 1/3[1120], while for TSD, the dislocation line is parallel to the Burger's vector, [0001]. As for TMD, as the name says, TMD is a mixture of TSD and TED with Burger's vector pf type 1/3[11-23]. Figure 1.4 shows schematic of the TED and TSD.

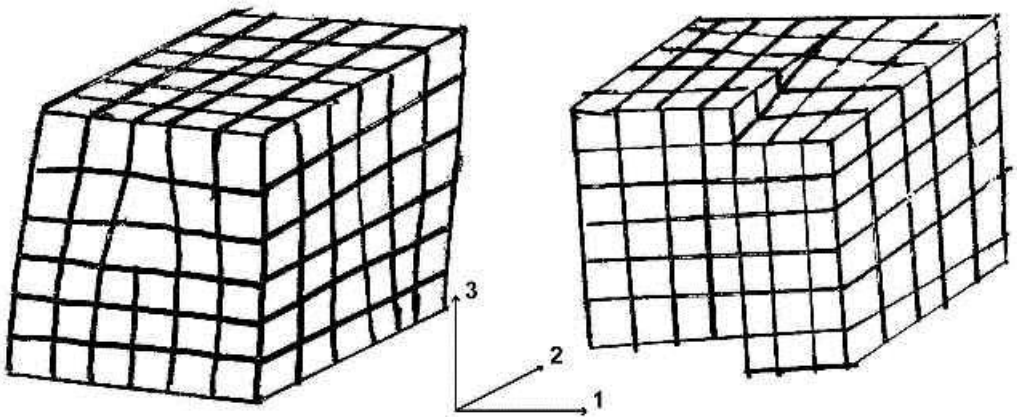

(a) (b)

Figure 1.4 (a) Screw dislocation and (b) edge dislocation.

1.2.3 Planar Defects

Planar defects comprise high and low angle boundaries, growth striations, growth sector boundaries, twin boundaries, stacking faults and antiphase boundaries [9]. The high and low angle grain boundaries are arrays of dislocations, especially threading dislocations, and then they will separate the regions of different orientations.

1.2.4 Volume Defects

For this group, the inclusions, precipitations and voids can be taken as volume defects. Inclusions are always from the solidification process when excess components exist. Precipitates are formed due to the retrograde solid solubilities of the components in the compound at lower temperature [9]. As for the voids, they can be formed when the gases dissolved in the melt precipitate.

1.3 Properties and Applications

With the development of nitride semiconductors, they have more applications in short wavelength optoelectronic devices and electronic devices in extreme environments.

1.3.1 AlN

Aluminum nitride (AlN) is a nitride of aluminum. It is a wide band gap (6.01-6.05 eV at room temperature) semiconductor material as shown in Figure 1.5, making it promising material in the application of deep ultraviolet optoelectronics. In fact, the existence of AlN was discovered as early as 1862 by F. Briegler and A. Geuther. And in 1877, J.W. Mallets achieved

the first synthesis. Until 1984, after more than a hundred years, AlN ceramic technology evolved quickly in industry. However, due to poor quality powders as well as inexperienced operating procedure, the AlN based products were best described as inconsistent. With more concerns arose, such as oxidative stability, hydrolytic stability, electric conductivity, thermal conductivity, thermal expansion, more and more researchers were attracted into this area, in this way, high-quality AlN substrates and devices emerged in the early 1990s. Compared with earlier AlN products, both the consistency and processing technique have been developed considerably.

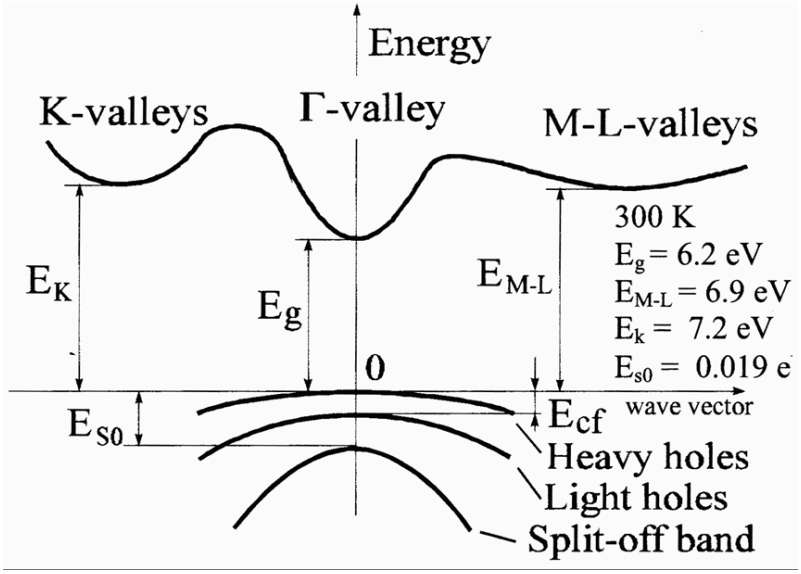

Figure 1.5 Band structure of AlN (Wurtzite).

Aluminum nitride has good stability at high temperatures in inert atmospheres and melts at 2800 °C. In a vacuum, AlN will decompose at temperature as high as 1800 °C. In the air, AlN can't be oxidized up to 1000K, and even when temperature is over 1000K, there will be a protective layer Al_2O_3 growing on the surface to prevent more oxidization. For AlN, the enthalpy of formation is -240.2 kJ/mol, the melting point under the condition of nitrogen pressure is near 2200 °C. Because of its low compressibility, good thermal stability, chemical and radiation inertness, AlN has more and more applications such as short-wavelength light emitting diodes, optical detectors, high-pressure, high-temperature, and high-frequency optoelectronic devices.

1.3.2 GaN

GaN shows many others superior properties compared to other semiconductor materials, such as high breakdown field of approximately 5×10^6 V/cm as compared to 3×10^5 and 4×10^5 V/cm for silicon (Si) and gallium arsenide (GaAs) (Morkoc et al., 1994). GaN is also a very stable compound. Its chemical stability at elevated temperatures coupled with wide bandgap has made GaN an attractive material for device operation in high temperature and caustic environments [4].

1.4 Growth Method

1.4.1 AlN

For different purposes, we may grow AlN with several methods, such as metal organic vapor phase epitaxy (MOVPE), hydride vapour phase epitaxy (HVPE), physical vapor transport (PVT) or the sublimation–recondensation method. For bulk growth, PVT is the dominant method.

The sublimation–recondensation method, which was first developed by Slack and McNelly, has been conducted as a promising way in order to obtain large bulk AlN boules. In this method, as a driving force, the thermal gradient motivates polycrystalline AlN to sublimate. The sublimation–recondensation process can be described by the following simple reaction:

$$AlN\ (s) \leftrightarrow Al\ (g) + \tfrac{1}{2}N_2\ (g) \qquad (1)$$

In this case, the polycrystalline AlN is starting material. And at the colder part of the crucible as a single crystal the recondensation occurs. As for the driving rate, it's influenced by a relative movement between the thermal gradient and the crucible. In the condition of adequate growth environment, including gas pressure and temperature gradient, the growth rate of a single crystal will be as same as the driving rate. However, because of improper conditions, platelets or polycrystalline material may result for a given driving rate. Since no seed is used in this method, during the first stage of the growth, there will be some nuclei forming on the crucible walls. Ideally, a single nucleus will form at the colder end of the crucible and, then, evolve into a large single crystal grain. Nevertheless, typically several nuclei will form and compete as the growth run proceeds [10]. From this process, the critical step and the grain selection will have a big effect on the resulting single crystal's quality, size and the amount.

Metal organic vapor phase epitaxy (MOVPE) methods are a subset of the wider family of chemical vapour deposition (CVD) processes, and the term refers specifically to processes in which layers with monocrystalline character are deposited on single-crystal substrates: a prerequisite for most advanced device applications [11]. This method for the nitrides is a fundamentally chemical process. It's usually conducted in continuous flow systems, and using simple metal alkyl precursors to react with ammonia. With the development of the method, it is always applied in the area of growth of complex multilayer structures for electronic devices. Even though MOVPE is a chemical process, it has been widely used in the research of applied physics, materials science, nano-science or crystal growth literature.

The AlN physical vapor transport (PVT) process contains the sublimation of a powder or polycrystalline AlN source below the triple point in a closed or semi-open crucible in a nitrogen ambient of several hundred mbar [12]. For the vapor transport process, the vapor will be transported along a temperature gradient, in which the direction should be from the source reservoir to the recrystallization zone. There is a case that source reservoir is in the lower side of the crucible compared with the recrystallization, then a vertical set-up is needed to keep the transportation going properly. For this process, AlN seeded growth was carried out in a reactor, as shown in Figure 1.6 [13].

PVT process can be subdivided into several steps as following:

(1) Sublimation of the AlN source material.

(2) Mass transfer of the vapor species.

(3) Adsorption of the vapor species at the growth surface.

(4) Surface diffusion and nucleation.

(5) Desorption.

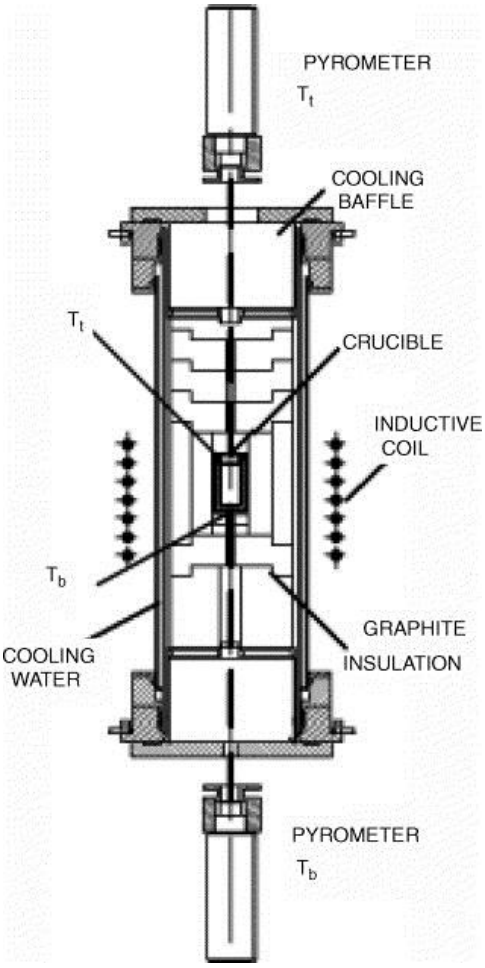

Figure 1.6 Schematic of the RF-heated AlN reactor.

For the industry, we need relatively low dislocation density, as a result, physical vapor transport (PVT) can be a better choice compared to others.

1.4.2 GaN

In order to reduce the amount of defects in crystal, many researchers have taken a big effort to grow the GaN by different kinds of ways, including the Na-flux method, high- pressure solution growth, hydride vapour phase epitaxy (HVPE), metallo organic vapour phase epitaxy (MOVPE), molecular beam epitaxy (MBE) and ammonothermal growth. From recent references, it's known that the ammonothermal GaN growth method can be efficient and feasible.

The Na-flux growth method has potential since much lower temperatures and pressures are sufficient and may simplify the crystal growth apparatus, thus promoting mass production of

bulk nitride crystals [14]. In usual, the starting materials for Na flux growth method of gallium nitride crystals were Ga and NaN_3 powders. After the staring materials preparation, they will be put into a reacting tube. The tube will be heating up to about 800°C. At approximately 300°C, NaN_3 decomposes into Na and N_2 gas [14]. As the temperature going up, more and more N_2 gas will be in the reacting tube. As a result, the pressure in the tube will increase. And the reaction will continue until the temperature is 800 °C. The nitride crystals were then extracted from the products with the Na residual removed by reaction in 2-propanol and then in ethanol [14].

The high pressure high temperature growth method is a classical way to get at least one group III single crystal. The method includes the steps of: providing a flux material and a source material comprising at least one Group III metal selected from the group consisting of aluminum, indium, and gallium, to a reaction vessel; sealing the reaction vessel; heating the reaction vessel to a predetermined temperature and applying a predetermined pressure to the vessel [15]. During the reaction, the pressure should be sufficient to process the group III nitride decomposition at the temperature.

The ammonothermal method is analogous to the hydrothermal method used to mass produce quartz, except that in the ammonothermal method ammonia is used as a solvent instead of water. The growth process is shown in Figure 1.7: GaN feedstock is dissolved in the upper part of the autoclave and transported to the seed crystals in the bottom part of the autoclave by convection, and crystallization occurs because of supersaturation of the solution [16]. Mineralizers are used to enhance GaN solubility in ammonia and determine whether the process environment is basic or acidic and if the resulting crystal structure is cubic or hexagonal. The temperature difference between the GaN seed and feedstock regions is positive in the ammonobasic regime and negative in the ammonoacidic regime. Ammonothermal crystals studied in publications I, II and IV were grown under ammonobasic conditions with alkali ($LiNH_2$, $NaNH_2$ or KNH_2) mineralizers. The crystal in publication III was grown with a sodium based mineralizer in a basic ambient.

There is a promising method that can get low dislocation density GaN substrates, these GaN substrates that will be grown by HVPE on ammonothermal GaN substrate, and then slicing the substrate. This combination of HVPE and ammonothermal method can give a good way for us to get a low defect density GaN.

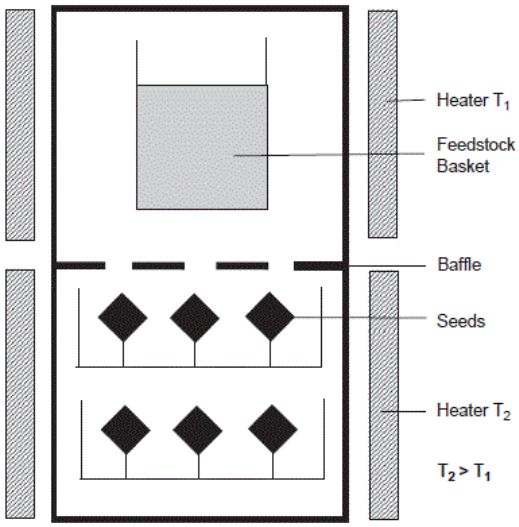

Figure 1.7 Schematic representation of the ammonothermal GaN growth method. GaN feedstock is dissolved in ammonia and transported to the seed crystals by convection. The dissolved GaN crystallizes at the seed surface.

Chapter 2.Characterization Techniques

2.1 Synchrotron X-ray Topography

Synchrotron radiation X-ray topography (SR-XRT) is a convenient and non-destructive characterization method suited for materials with dislocation density~$10^6 cm^{-2}$and below [17]. Synchrotron radiation can directly provide an intense beam with very low divergence, that enables rapid imaging of large area samples. Compared with traditional topography synchrotron, X-ray topography has numerous advantages.

2.1.1 Development of XRT

As early as 1895, Wilhelm Rontgen discovered X-ray, at that time, it was a completely new discovery for scientists. For a long time after the discovery, researchers were looking up ways to take advantage of this fantastic technique. Even though the first topographic image of a single crystal was recorded as early as 1931 (Berg, 1931), the real potential of the technique was understood only in 1958 when Lang (1958) demonstrated the imaging of individual dislocations in a silicon crystal. Different topographic geometries were developed independently during this period [18].

(1) Berg–Barrett reflection technique (Berg, 1931; Barrett, 1945).

In 1931, Berg conducted a reflection geometry to image the crystal surface characterization. In this experiment, the radiation fell at a really low angle to the crystal surface. In this way, Berg obtained the images of the reflected intensity. Then in 1945, another scientist Barrett wanted to make some improvement on Berg's reflection technique. As a result, by adjusting the alternative distance between crystal and photographic emulsion plate, he firstly recorded the defects structure of single crystal silicon ferrite. This can be described as a significant stage for the modern X-ray topography technique.

(2) Double-crystal technique (Bond and Andrus, 1952)

In this case, X-rays source will be Bragg-reflected from a highly perfect monochromator crystal, and after the Bragg reflection the X-ray will be diffracted by sample crystal, both reflection and transmission can be achieved. What's more, because of the highly perfect monochromator crystal, the divergence of the beam can be narrowed effectively. In this way, the double-crystal technique can be considered as a high sensitive technique.

(3) Lang technique (Lang, 1958)

During 1957, Lang was trying to employee a narrow collimated radiation beam to characterize the crystal. By doing this, he was able to observe and record the defects in crystal and it is also a kind of transmission, and this technique is a mixing up between projection and section topography. The advantage of this technique is that it can detect and record the linear and planar defects in crystal, it's a good way for us to study the crystal.

(4) Synchrotron X-ray topography

The advent of dedicated sources of synchrotron radiation has enabled the development of a new realm of topography known as synchrotron topography.

2.1.2 Introduction of Synchrotron XRT

The synchrotron was originally developed for research in high energy particle interaction with matter, but was found to emit electromagnetic radiation with a continuous wavelength spectrum, very low divergence and high brilliance. The charged particles are decelerated in the curved parts of the storage ring, emitting soft X-rays in a narrow cone in the tangential directions [19]. Because the unique properties of synchrotron radiation, such as continuous spectrum, high flux and brightness, and high coherence, it plays a significant role during the research process. The wavelengths of the emitted photons span a range of dimensions from the atomic level to biological cells, thereby providing incisive probes for advanced research in materials science, physical and chemical sciences, metrology, geosciences, environmental sciences, biosciences, medical sciences, and pharmaceutical sciences. The features of synchrotron radiation are especially well matched to the needs of nanoscience.

The fundamental parameters that we use to perceive the physical world (energy, momentum, position, and time) correspond to three broad categories of synchrotron experimental measurement techniques: spectroscopy, scattering, and imaging. By exploiting the short pulse lengths of synchrotron radiation, each technique can be performed appropriately. The schematic figure for the synchrotron radiation ring is shown below, which is from Argonne National Laboratory.

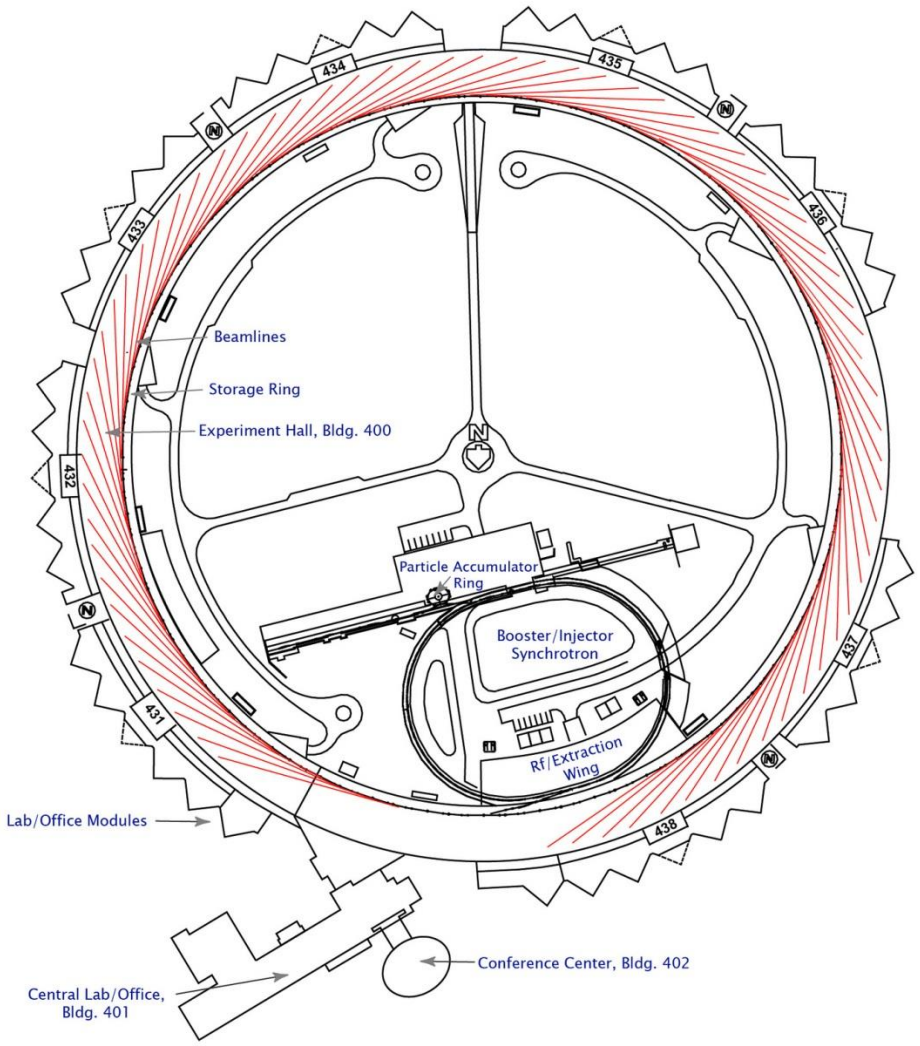

Figure 2.1 The Advanced Photon Source (APS) synchrotron X-ray ring at Argonne National Laboratory.

2.1.3 Applications of Synchrotron XRT

With the help of synchrotron X-ray topography, it's convenient to 'see' the defects inside crystals at a high resolution. There are several setups to image different kinds of defects, such as transmission geometry, back-reflection geometry and grazing geometry.

(1) Transmission

As the schematic figure shown below (Figure 2.2), the direct beam will go through the sample and then we can observe the Laue spots on the recording plate. By comparing the spots on the recording plate with the standard spots from Laue Pattern, we can index that spots. Enlarging each spot will reveal defects in the crystal sample.

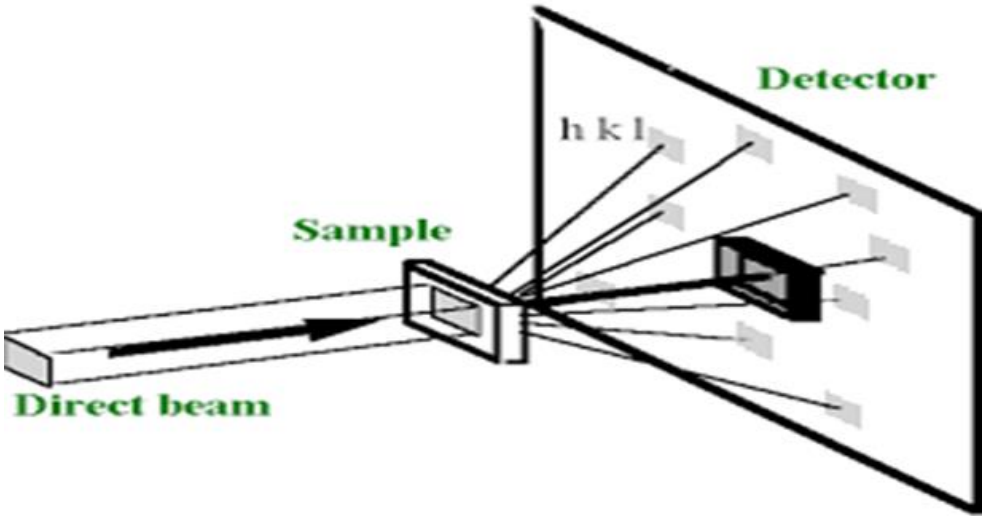

Figure 2.2 Schematic for Transmission geometry X-ray topography.

Each set of planes in the crystal (of given d spacing) chooses its own λ from the beam such that the Bragg law is satisfied, in this way each diffracted beam has different λ [20]. Spots actually lie on curves, ellipses or hyperbolae for transmission patterns. In the Transmission technique, the tendency is to exaggerate the effect of the rotation of the plane normal in the direction parallel to the plane of incidence, compared with directions perpendicular to the plane of incidence. Usually, we can record [11-20] or [1-100] plane to get the basal plane dislocations (BPD), which is of significance during the defects study of III-nitrides.

(2) Back Reflection

Spots actually lie on hyperbolae or straight lines for back reflection patterns, the schematic is shown below (Figure 2.3) [21]. Distance of any hyperbola from the center of the film is measure of the inclination of the zone axis. Back reflection technique is especially useful for determining the orientation of crystals and deducing the morphology of large solution grown single crystals. Back reflection technique is preferred in studies of lattice distortion. Back reflection technique has also been used to measure lattice rotations of crystal undergoing plastic deformation. Back reflection topography has been used to image threading screw dislocations in SiC and GaN.

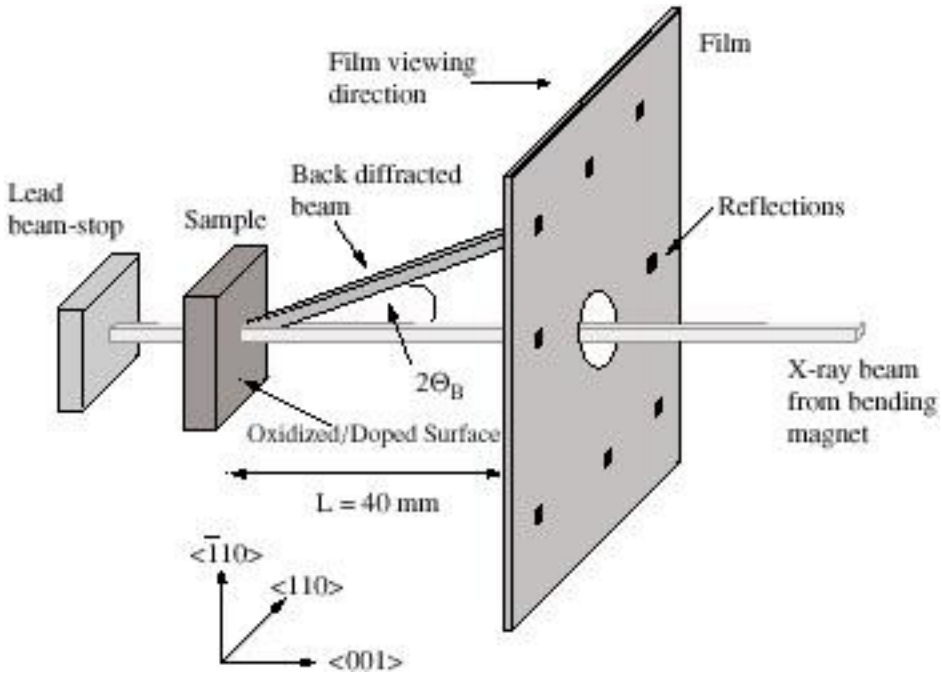

Figure 2.3 Schematic for back reflection.

(3) Grazing Incidence

In this case, grazing incidence geometry is very sensitive to surface features. For different kinds of crystals, we can set different incident angles in order to get the information. From grazing incidence, it's convenient for us to obtain images of threading dislocations (TDs) in the crystals. Compared with transmission geometry, the grazing incidence geometry's penetration depth is limited to the order of several microns.

As the schematic shown above, our experiment grazing geometry is a little different from that, besides the diffraction angle and film position, as shown in Figure 2.4:

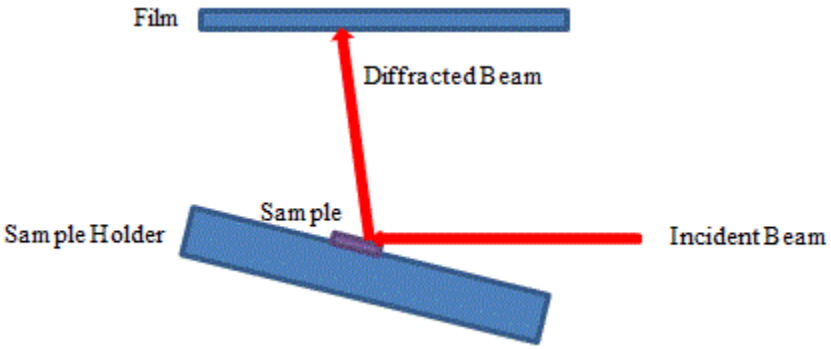

Figure 2.4 Our experiment grazing incidence geometry.

2.1.4 Image Contrast

In order to get some information from the topography images, the contrast of the images are always being considered. Besides the grey background, some white or dark contrast can be detected from the films (as shown in Figure 2.5).

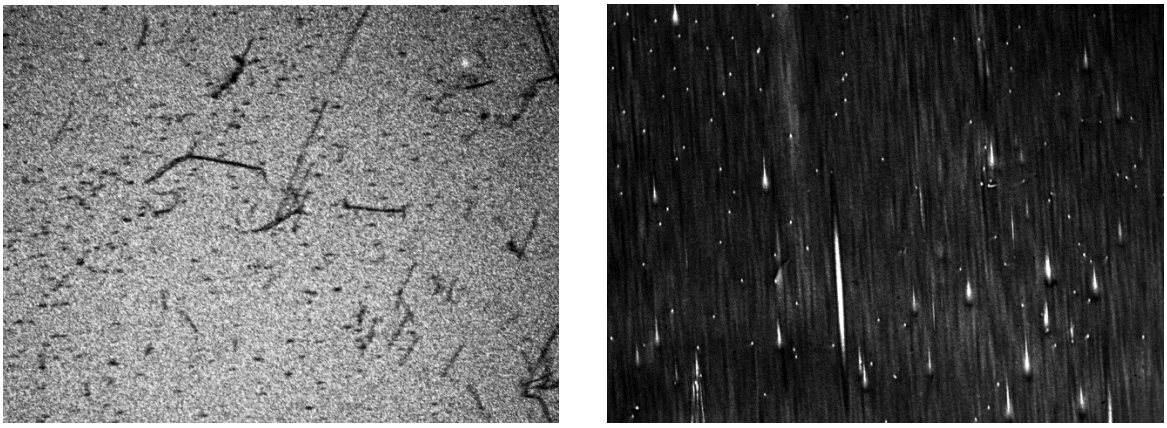

(a) (b)

Figure 2.5 X-ray topography images (a) white beam X-ray (b) monochromatic beam X-ray with the area 2.3mm×1.7mm.

The contrast is the result from the interaction between the incident X-ray beam and the distortions of the diffracting lattice planes. In this way, from the images contrast, the properties of the incident beam and the specimen can be observed. The dominant contrast formation mechanism strongly depends on the defect type and density, crystal properties and dimensions as well as the type of X-ray source, the instrumentation and the specific experimental technique [9].

There are two main mechanisms for the image contrast in X-ray topography: (1) orientation contrast and (2) extinction contrast.

(1) Orientation contrast

In the condition of misorientation, like grain boundaries, twins, the orientation contrast can be observed as a result of orientation change. Meanwhile, the occurrence of orientation contrast can be affected by the nature of the X-rays. For different cases, it is demonstrated as below:

I. Synchrotron white beam radiation

From the Bragg's Law, in the same atom plane without defects, the Bragg angle is the same when given an incidence X-ray. Therefore, the diffracted beam should also exit from the sample surface in the same direction. So if the crystal is illuminated by continuous radiation such as the synchrotron white beam, regions of different orientation select different wavelength from the broad white spectrum for diffraction leading to a superposition of several different sets of diffraction patterns [9]. The schematic figure is shown below:

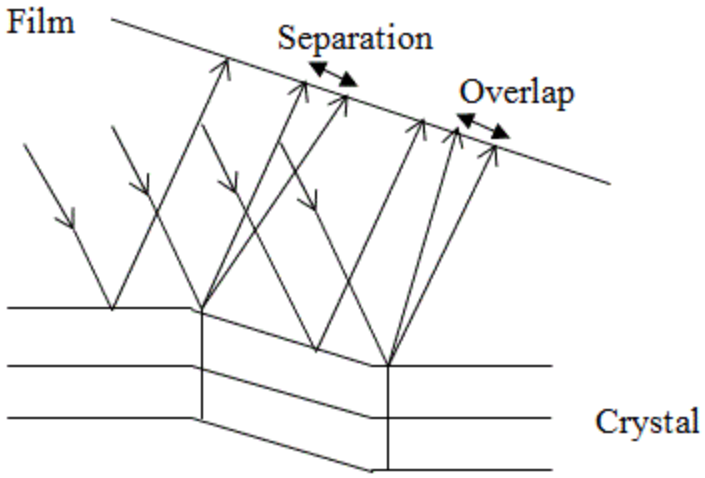

Figure 2.6 White beam radiation.

II. Monochromatic beam radiation

Similarly, the misorientation of the crystal and the beam divergence can diffract, and then get the image. Depending on different types of defects, the diffracted beam can exit from the sample in different directions; result in overlapping or separation (as shown in Figure 2.7).

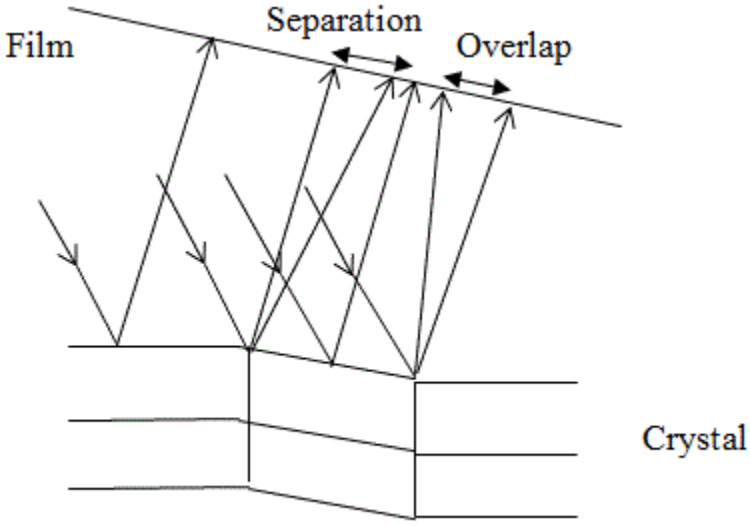

Figure 2.7 Monochromatic beam radiation.

(2) Extinction Contrast

When the scattering power around the defects is different from that in the other parts of the crystal, as a result of this, extinction contrast can take place. And the extinction contrast contains three components: direct image, intermediate image and dynamic image. For these three

components, each one can be dominant depending on the absorption. The absorption here is measured by the crystal's absorption coefficient μ and crystal's thickness t. When $\mu \cdot t<1$, it means the absorption of the crystal is relatively low, in this case, the direct image can be the dominant contrast. For $1<\mu \cdot t<4$, the main contrast can come from the intermediate image. In the case of $\mu \cdot t>4$, meaning a high absorption condition, then the dynamic image is the dominant contrast.

2.2 Optical Microscopy

During this study, besides X-ray topography experiments, another useful characterization technique utilized Nomarski optical microscopy (Figure 2.8), with Nikon Polarizing Microscope Eclipse E600W POL. Since the microscope has a resolution of nearly 0.1 micron, both the sample's surface morphology and occasionally the defects inside the sample can be detected clearly by this microscope.

Figure 2.8 Nikon Polarizing Microscope Eclipse E600W POL used for Nomarski optical microscopy.

Chapter 3.Study of Defects in AlN and GaN crystals

3.1 Introduction

In this chapter, the analysis of AlN and GaN samples will be discussed in detail. By means of synchrotron X-ray topography in transmission and grazing geometry, high resolution images of these samples have been recorded. Therefore, it's a good way to study the basal plane dislocations (BPDs) and threading dislocations (TDs). Then, by comparing the dislocation density among similar samples, some important properties can be gotten from these images.

3.2 Experiment

3.2.1 AlN

The synchrotron X-ray topography experiments were conducted at Advanced Photon Source, Argonne National Laboratory. In our experiment, the white beam and monochromatic beam are employed to image samples. Usually, we use white beam to record the basal plane dislocations (BPDs), and monochromatic beam to record threading dislocations (TDs). For white beam size we use is about 43mm×1mm, and the largest AlN samples are about 25mm in diameter. Thus, the beam size is large enough to cover the whole wafer. A single vertical scan is sufficient for the AlN samples. If the size of sample is larger than the beam size, we need to carry out several separate scans in order to get the whole area images. For example, in order to cover the whole wafer, we separate the wafer into three parts, I, II and III (Figure 3.1). And then for each part, we can scan it from top to bottom. In this way, we can get the whole images of the wafer. And for the monochromatic beam, we need to check the contour first, and then make an assumption about the whole wafer to decide the total number of contours required to cover the wafer.

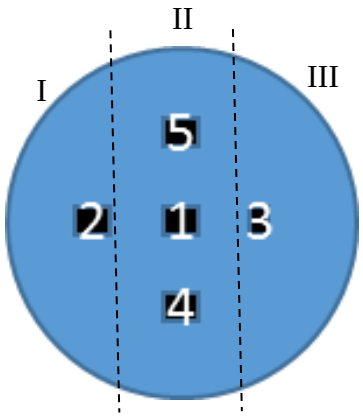

Figure 3.1 Different parts of a wafer.

In order to get the dislocation density, we should know that dislocation density is the total length of dislocation per unit volume or the total number of dislocation intersecting sample surface per unit area. Usually, the unit of dislocation density is cm^{-2}. In this way, we get two kinds of formulas to calculate the density:

$$\rho = l/(S \cdot t) \qquad (1)$$

In which, ρ is the volumetric dislocation density, S is the area with dislocation, t is the thickness of the sample.

$$\rho = N / S \qquad (2)$$

In which, ρ is the areal dislocation density, N is the total number of dislocations intersecting the surface, S is the area with over which dislocation counts are carried out.

3.2.2 GaN

The GaN samples, sizes are of order of 10mm, much smaller than the AlN samples. Therefore, the sample is mounted between two cardboards with kapton covered cutouts. By doing this, we can ensure the sample is tightly held and does not move. Then, similar to AlN sample, we need to scan the whole sample vertically from top to bottom in order to get the whole image of the wafer. In the grazing case, we need to make a estimation about the diffracted angle and then get several contours to cover the wafer.

3.3 Result and Discussion

3.3.1 AlN

Sample 1--AlN-1

(1) Transmission topography

By white beam synchrotron X-ray topography, we can get the transmission topography shown below (Figure 3.2), with diffraction vector $\vec{g}$ = [11-20] and [1-100] respectively. Since the thickness of sample is just a few hundred micrometers, we need to use some precise measuring tool to get the thickness, in our experiment, the micrometer screw is employed. The thickness was measured to be 394 microns. The topograph shows below:

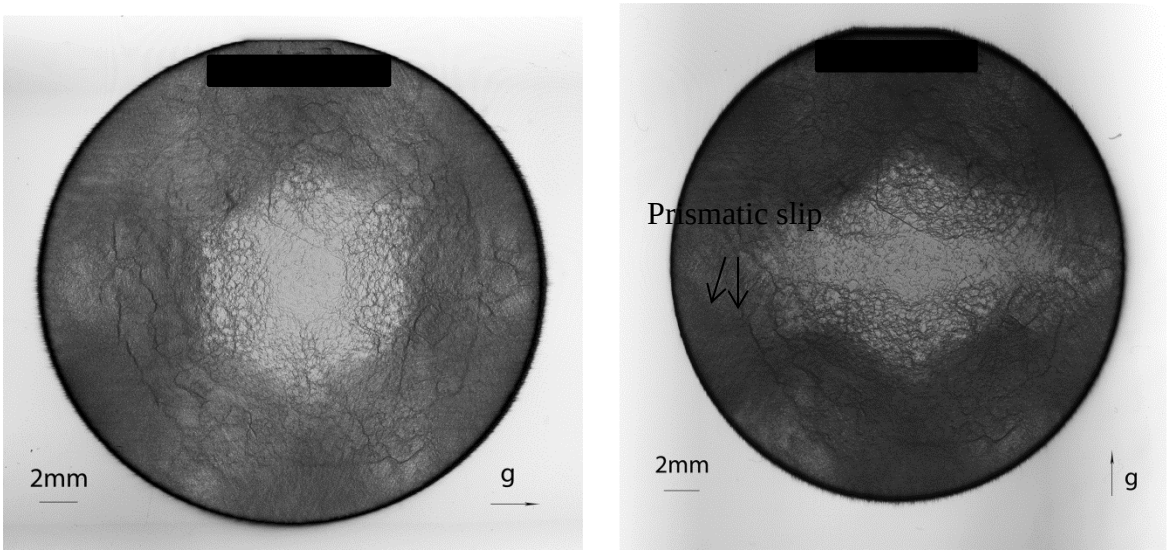

(a) (b)

Figure 3.2 Transmission topographs for (a) g= [11-20] and (b) g= [1-100] of AlN sample 1showing BPDs.

In order to get the dislocation density of the sample, we decide to select 5 positions to calculate the basal plane dislocation density from the diffraction vector [11-20] topography. The magnified images are taken using Nomarski optical microscope, and each rectangle is 2.3mm × 1.7mm. The approximate positions are shown in Figure 3.3.

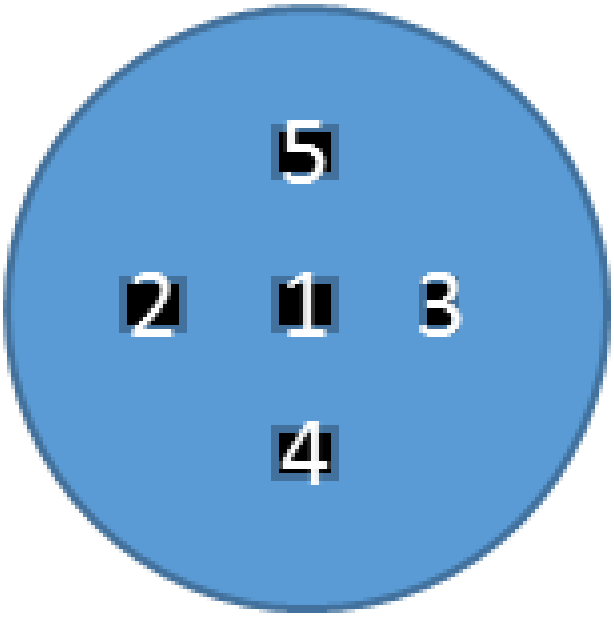

Figure 3.3 Approximate locations of high magnified images for dislocation counts.

From the dislocation density equation we can get the approximate density of each area respectively. These 5 magnified images are shown below (Figure 3.4):

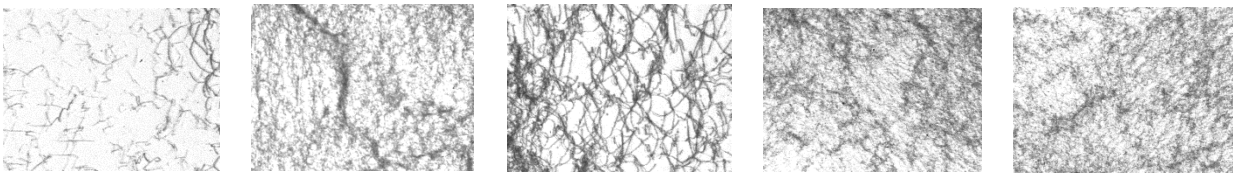

(1) (2) (3) (4) (5)

Figure 3.4 Magnified images of transmission topographs for 5 positions of AlN sample 1.

In order to get the dislocation density, we need to know the total length of the BPDs. In our experiment, the SPOT Application software is employed to measure the total length of BPDs in each position. In this way, we can get the basal plane dislocations (BPDs) density shown in the Table 3.1 shown:

Table 3.1 BPD density for 5 positions of AlN sample 1

Position	1	2	3	4	5
BPD density ($\times 10^4 cm^{-2}$)	0.357	2.430	1.980	2.360	0.608

The average density is 1.547 $\times 10^4 cm^{-2}$. From the density distribution we can get that, the density of central position (position 1) is much lower than the other position around the edge (position 2, 3, 4, 5). Correlation this with the growth process, we can get insights into the cause for this defect distribution. During crystal growth, due to the temperature gradients during

postgrowth cooling, thermal stresses in the boule can go over the critical resolved shear stress on the basal plane, thus BPD half-loops will nucleate at boule edge and begin to glide and propagate. BPDs are propagating from the edge of the wafer to the center, therefore, the BPD density is higher on the edge compared with those in center. Stress on the basal plane can have great effect on the resultant defect distributions. For example, like BPDs, it is the stress on basal plane that activates them to glide. For prismatic dislocations, the stress on prismatic planes is the main factor that makes them glide. There are many factors that can induce such kind of basal plane stress. One of the factors is the non-linear temperature gradient along the growth direction of the boule. This stress can induce deformation in the crystal leading to BPDs in the crystal. Besides the BPDs, some low angle grain boundaries (LAGB) can be found in the transmission images, as shown in Figure 3.5:

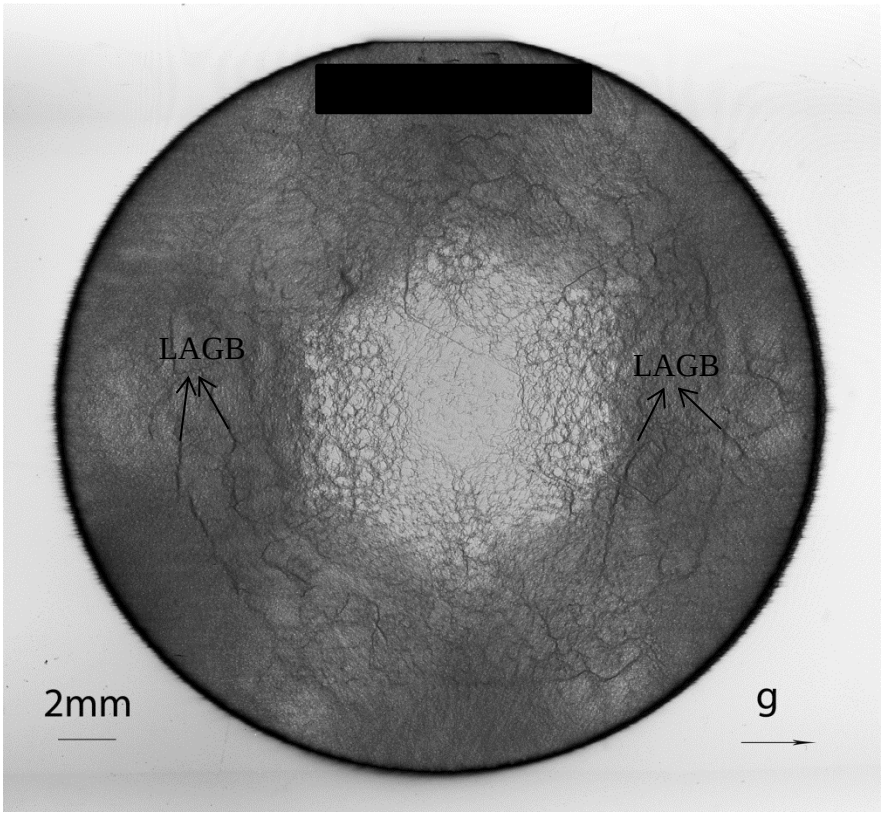

Figure 3.5 [11-20] transmission images with LAGB indicated of AlN sample 1.

As we can see from Figure 3.5, the LAGBs are revealed by orientation contrast—dark contrast due to overlap between subgrains. The LAGBs are composed of arrays of TEDs. These threading dislocations arrays can prevent the BPDs from gliding. As a result, these BPDs can accumulate around these TEDs arrays. This could also be a factor leading to higher- BPD density near wafer edge compared to center.

(2) Grazing incidence topography

By monochromatic beam synchrotron X-ray topography, we can get the grazing incidence topograph shown below (Figure 3.6) and the diffraction vector $\vec{g}$ = [11-24].

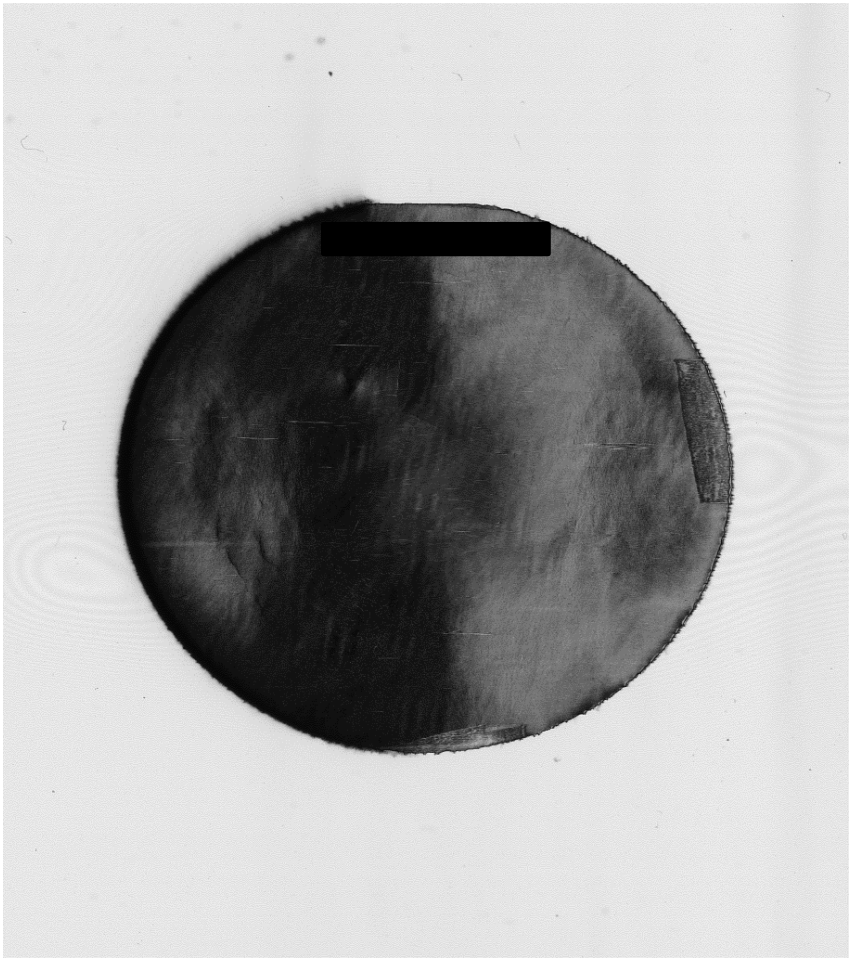

Figure 3.6 Grazing topograph [11-24] of AlN sample 1showing TEDs and TSDs.

For the grazing incidence topography, the Bragg angle is 41.5˚, and, TED, TSD, TMD can be observed from diffraction topohraph. From the grazing incidence geometry we know that the incident beam is at a very small angle with the surface, therefore, the incident beam does not pass through the whole wafer. Usually, the penetration depth is about a few micrometers. In other words, in grazing topography, we observe the defects in a few micrometers from the surface. Half of the wafer is covered by about 2 sets of contour indicating small curvature in the wafer and low residual stresses. We select 3 positions from the images to get the magnified images using Nomarski Optical Microscope, with rectangle at 2.3mm × 1.7mm, as shown in Figure 3.7.

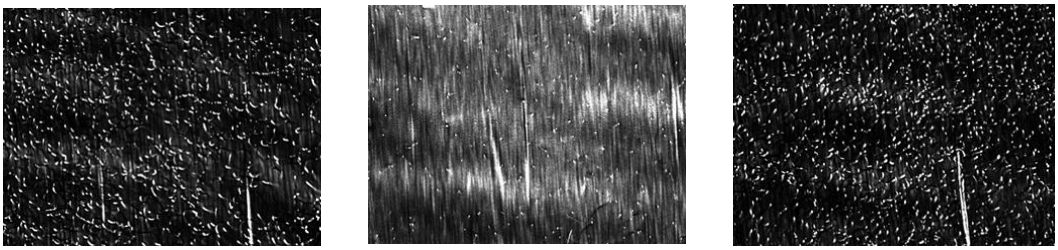

(1) (2) (3)

Figure 3.7 Magnified images of grazing incidence topographs for 3 positions of AlN sample 1.

By counting the number of TDs of each area, we can get the threading dislocation density, as shown in Table 3.2.

Table 3.2 TDs density for 3 positions of AlN sample 1

Position	1	2	3
TDs density ($\times 10^4 cm^{-2}$)	0.51	0.88	1.34

There are mainly two types of threading dislocations, including threading screw dislocation (TSD) and threading edge dislocation (TED). The chief criterion to distinguish TEDs from TSDs is that TED images have a symmetrical shape, while TSD images do not [22]. In usual, the size of TEDs can be much smaller than TSDs. And it is clear that the dislocation density of the central part is lower than the edges.

Sample 2—AlN-2

(1) Transmission topography

This sample is also similarly imaged and the transmission images are shown below, and we can also get the thickness for this sample, is 386 microns.

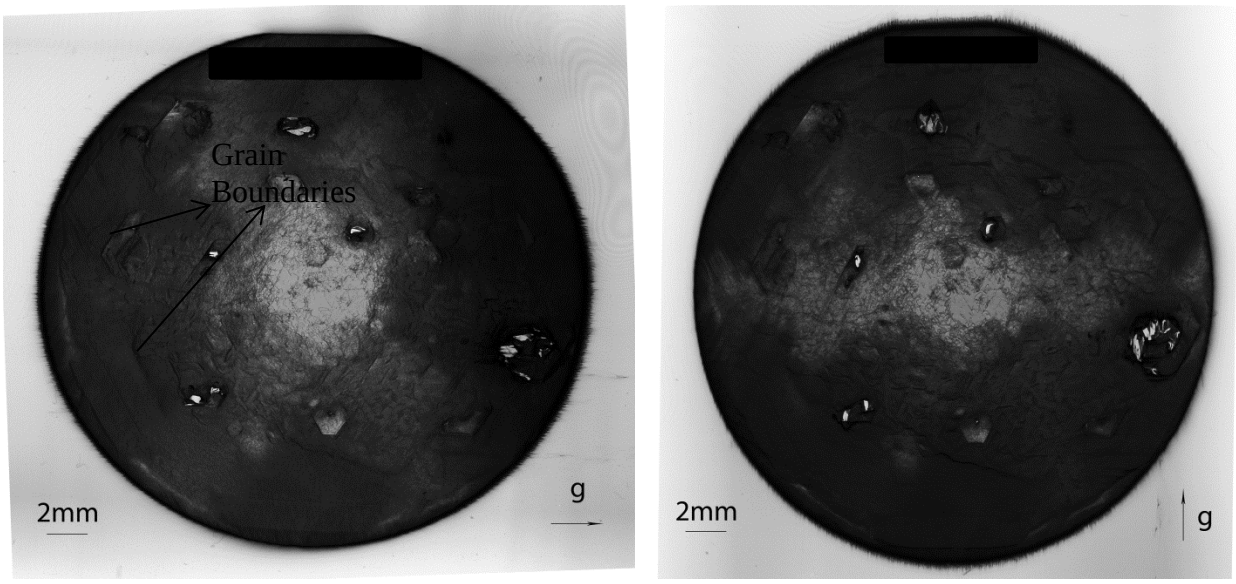

(a) (b)

Figure 3.8 Transmission topography for (a) g = [11-20] and (b) g = [1-100] showing BPDs.

Also, we get the magnified images for 5 different positions as below from the microscope.

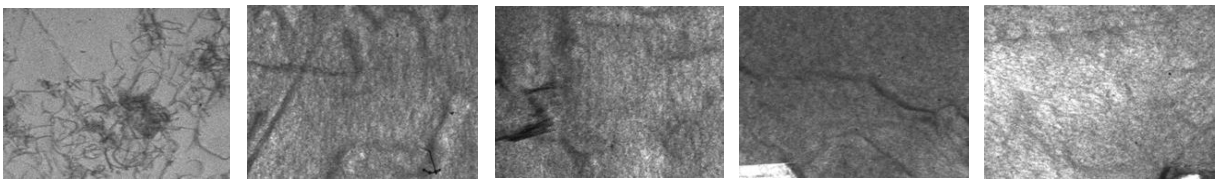

(1) (2) (3) (4) (5)

Figure 3.9 Magnified images of transmission topographs for 5 positions.

And then we can get the BPDs dislocation density for 5 different positions as the Table 3.3 shown below:

Table 3.3 BPD density for 5 positions

Position	1	2	3	4	5
BPD density ($\times 10^4 cm^{-2}$)	0.776	1.833	1.425	1.198	1.558

The average of BPD density is about $1.3568\times10^4 cm^{-2}$. It's clear to see that the BPDs density of center is lower than that around edge. We can also get the information that the BPDs are propagating from the edge of the wafer to the center. BPDs and possibly TEDs have formed low angle grain boundaries (LAGBs) in some regions through the process of polygonization glide and climb of dislocations to form tilt boundaries.

For this sample, we can observe some hexagonal shapes, and they mainly distribute around the edge of the wafer. These kind of hexagonal shapes are low angle grain boundaries. By

detailed study, we see that these grain boundaries are oriented along the <1-100> directions. These are composed of arrays of 1/3<11-20> TEDs and normally formed around clusters of TSDs.

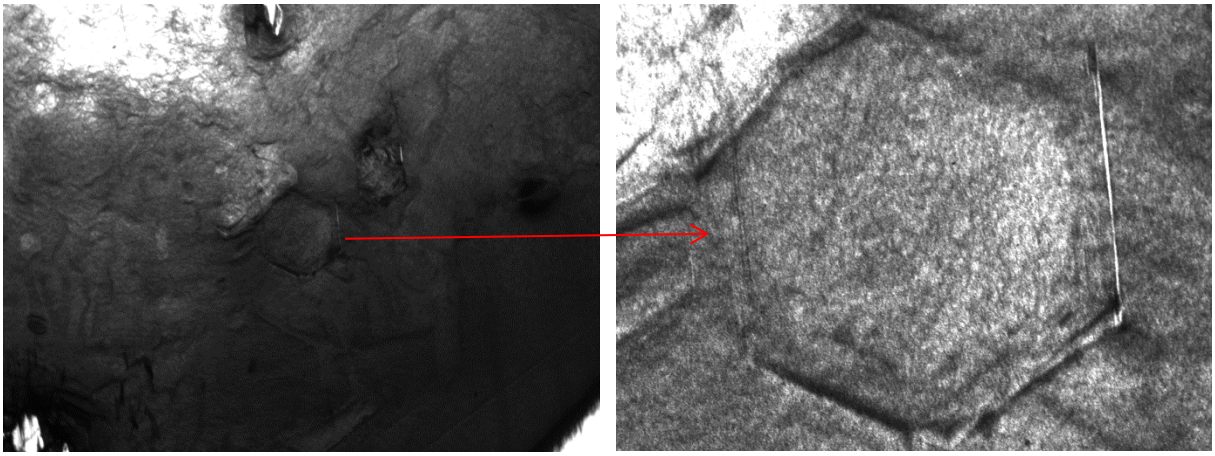

Figure 3.10 A hexagonal shape found in transmission image and its magnified image.

From the width of grain boundaries, we can get the tilt angle by using a formula:

$$\theta = 2\arctan(d/2D) \qquad (3)$$

In which, θ is the tilt angle, d is the grain boundaries width, and D is the distance between sample and film. In order to figure out the principle of the formula, we can use a schematic to illustrate the basic information about the tilt angle.

From the width of grain boundaries, we can get the tilt angle. For this sample, grain boundary width d is 0.0385mm, and in our experiment the distance between sample and beam D is 17cm. Then we can get the grain boundary tile angle is 0.7438˚.

(2) Grazing incidence topography

By monochromatic X-ray we can get the grazing incidence topograph, as shown in Figure 3.12.

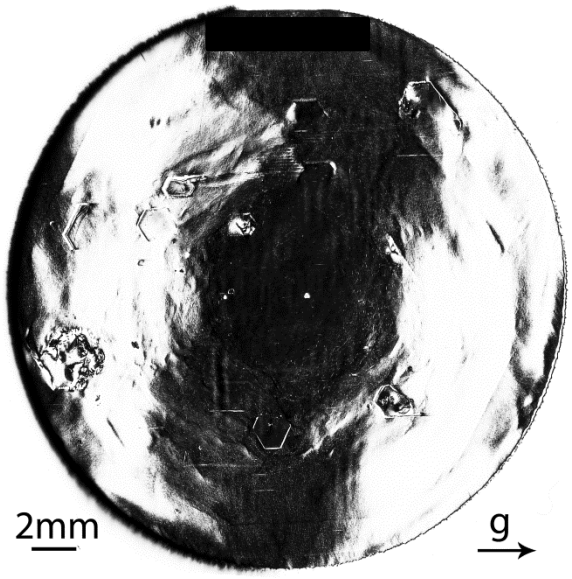

Figure 3.11 Grazing topography [11-24] showing TEDs and TSDs.

Most of the wafer is covered by about 3 sets of contour indicating small curvature in the wafer and low residual stresses. Meanwhile, we select 5 different positons to calculate the threading dislocation density, the 5 positions are the same as the transmission part in Figure 3.3. And then we use the Nomarski optical microscopy to get the magnified images, as shown in Figure 3.12.

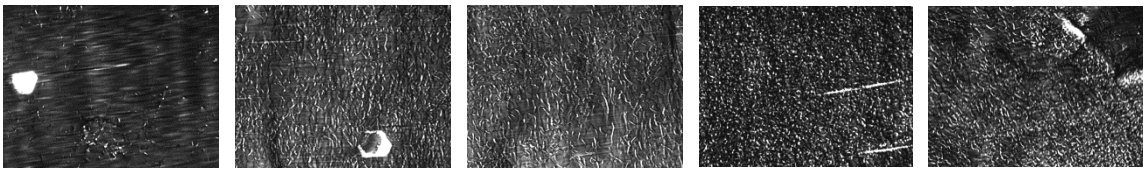

(1) (2) (3) (4) (5)

Figure 3.12 Magnified images of grazing incidence topographs for 5 positions.

The threading dislocation density is shown in Table 3.4.

Table 3.4 TDs density for 5 positions

Position	1	2	3	4	5
TED density ($\times 10^4 cm^{-2}$)	0.391	1.054	0.840	2.827	2.521
TSD density ($\times 10^4 cm^{-2}$)	0.166	0.520	0.458	1.650	1.604

From the Table we can get that, both in the case of TED and TSD density distribution, the density in the center is smaller than that around the edge. Also, for the reason that the images form the grazing incidence geometry is very sensitive to the defects and bending, even a little difference on the plane can cause the different performance on the film. In the grazing topography images, we can get some information from the dark regions. But for white or light

regions, we can hardly get anything from that. With the existence of the bending on the surface, the incident angle for these white regions can be out of the range of rocking curve angle range. As a result, these regions are not able to diffract the X-ray beam, then cannot form images on the film.

There are also some special hexagonal shapes around the wafer edge, we can use the microscope to record the magnified images as below:

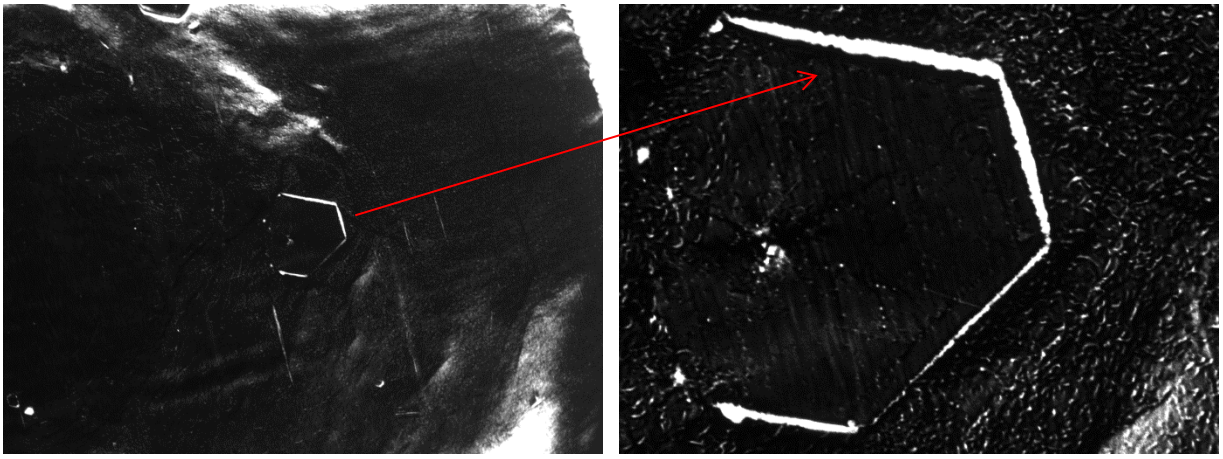

Figure 3.13 A hexagonal shape found in grazing image and its magnified image.

By observing the distribution of the grain boundaries, it's clear that most of the grain boundaries are around the edge of the wafer, and rarely can be observed in the center. For this sample, grain boundaries width d is 0.059mm, and in our experiment the distance between sample and beam D is 33cm. Then we can get the grain boundaries tile angle is 0.5872°.

Sample 3 – AlN-3

(1) Transmission topography

By white beam synchrotron X-ray topography, we can get the transmission topography shown below, and the diffraction vector $\vec{g}$ = [11-20] and [1-100] respectively. Since the thickness of sample is just a few hundred micrometers, we need to use some precise measuring tool to get the thickness, in our experiment, the micrometer is employed and the thickness is 388 microns.

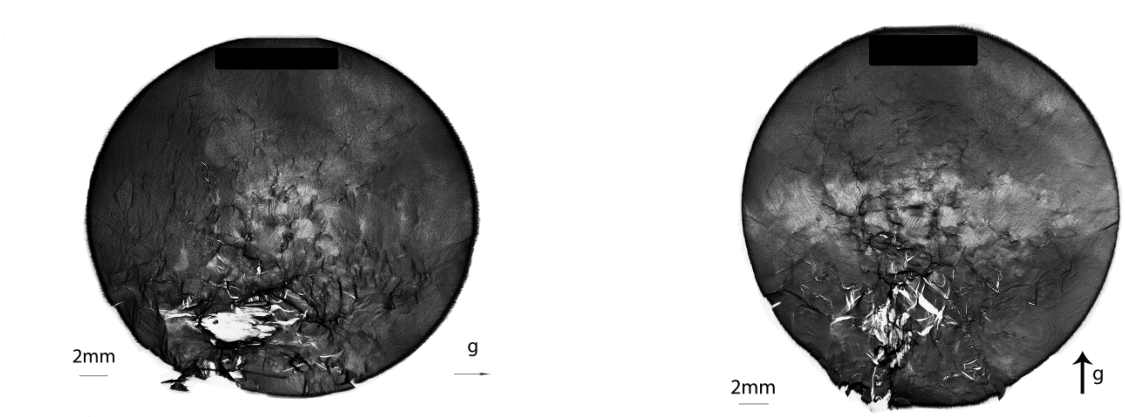

(a) (b)

Figure 3.14 Transmission topographs for (a) g = 11-20 and (b) g = 1-100 showing BPDs.

Wafer shows a network of basal plane dislocations (BPDs). BPD loops of each type of 1/3<11-20> dislocation are nucleated from different side surfaces of the boule and propagate into the boule under the influence of thermal gradient stresses during post-growth cooling. As we have discussed above, the BPDs are propagating from the edge of the wafer into the center. Then the dislocation density in the center is lower than that around the edge. On the [1-100] topograph shown above, dislocations of type 1/3[11-20] are invisible (g.b=0). BPDs and possibly TEDs have formed low angle grain boundaries (LAGBs) in some regions through the process of polygonization (glide and climb of dislocations to form tilt boundaries). From the topography images, there are some regions with high distorted white contrast. One of the possible reasons for these regions is that they contain large number of low angle grain boundaries (LAGBs). There might be also large inhomogeneous strains in these regions which can induce high distorted white contrast on the film.

Also, we get the magnified images for 5 different positions as below from the microscope.

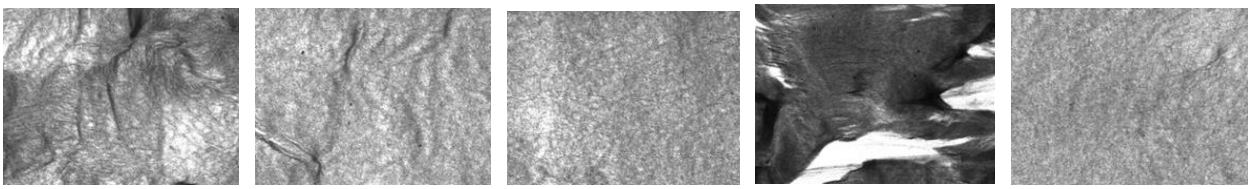

(1) (2) (3) (4) (5)

Figure 3.15 Magnified images of transmission topographs for 5 positions for sample 3.

And then we can get the BPDs dislocation density for 5 different positions as shown below:

Table 3.5 BPD density of 5 positions for sample 3

Position	1	2	3	4	5
BPD density ($\times 10^4 cm^{-2}$)	1.632	1.405	1.389	>10	1.336

The average of the density is over $3.1524\times10^{4}cm^{-2}$. For this sample, the BPDs density is relatively high. And except the position 4, which contains large inhomogeneous strains and large number of low angle grain boundaries, the dislocation density of other part distributes uniformly. The white contrast induce by the distortion has great effect on the observation of the dislocations.

There are also some networks of low angle grain boundaries around the wafer edge and using the microscope, we can record magnified images as below:

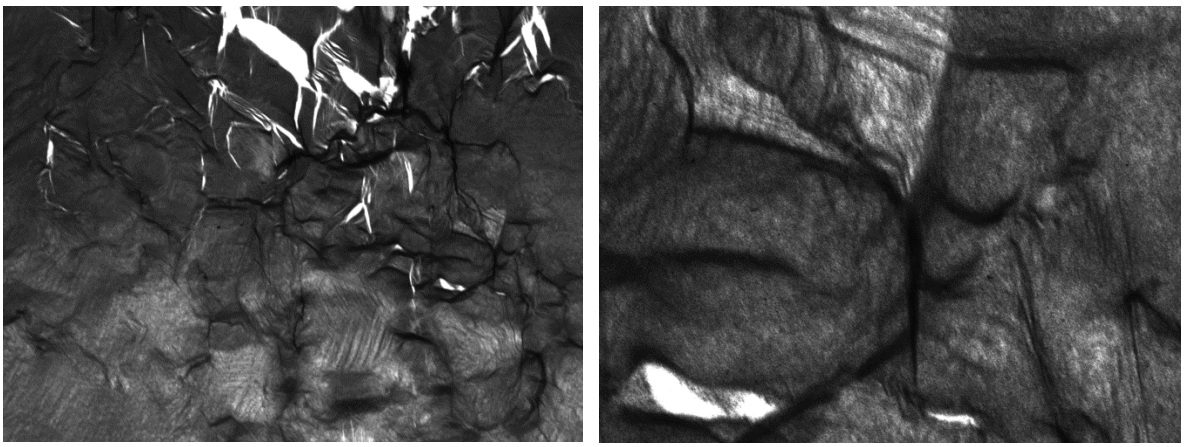

Figure 3.16 A special selected area in transmission image and its magnified image.

For this feature, the grain boundaries are close to the large strains area, so some white contrast can be observed from these images. And the grain boundaries are a little different from others, they are not straight as others. What's more, instead of regular hexagonal shape, their shapes are more complex. For this grain boundary, the width is about 0.0716 mm. And the tilt angle is 0.712˚.

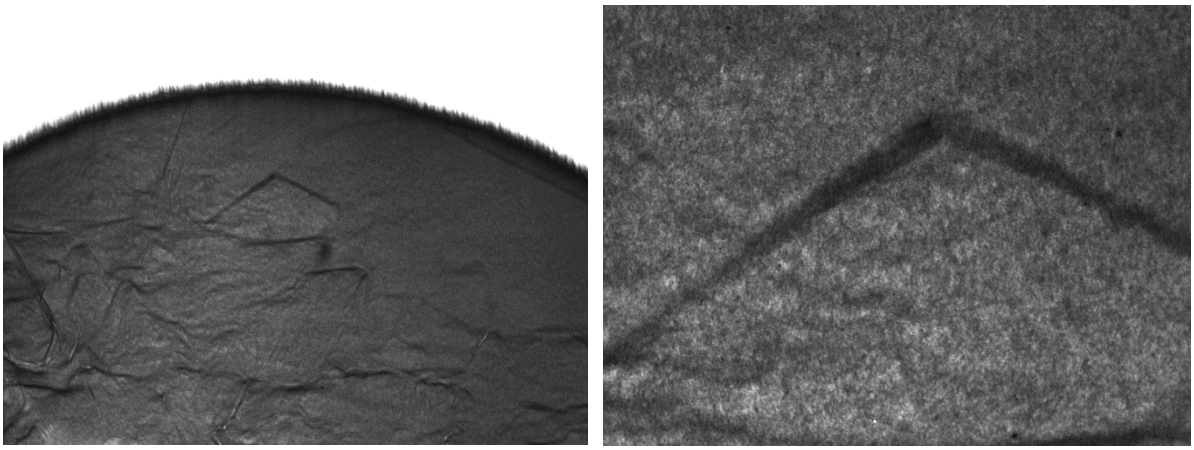

Figure 3.17 A special area in transmission image and its magnified image.

For this grain boundary, it is close to the edge of the wafer. We can observe the grain boundary from the images clearly and this grain boundary is like a straight line. Different from the grain boundary in Figure 3.16, this grain boundary located in a region with fewer strains and

less grain boundaries. For this grain boundary, the width is about 0.103 mm. And the tilt angle is 1.024˚.

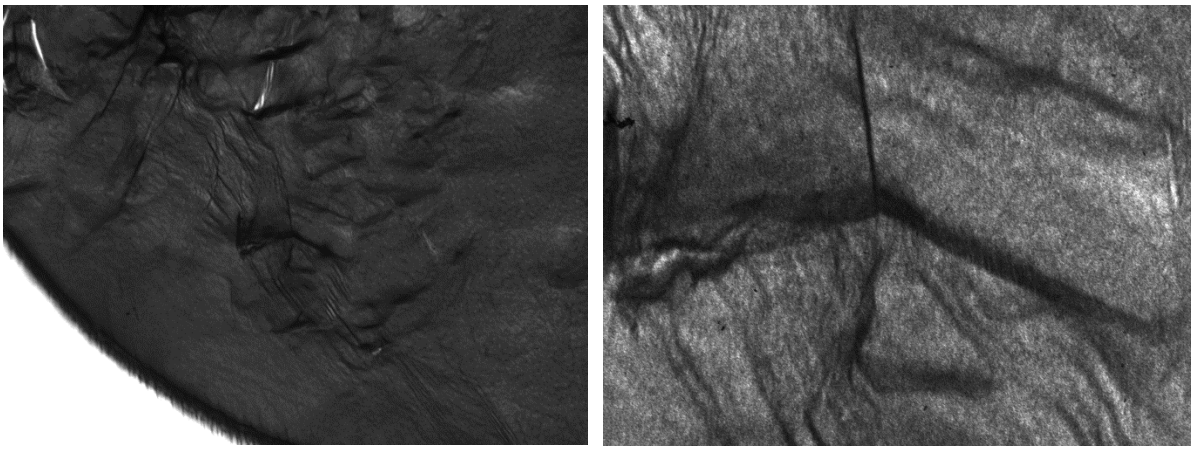

Figure 3.18 A special area in transmission image and its magnified image.

This grain boundary is a case between the first one and the second one, it is located in a region with a few strains. There are a few grain boundaries interacting with each other, and some of them can also be a straight line, others may be curved due to the strains in that region. For this grain boundary, the width is about 0.0815 mm. And the tilt angle is 0.8107˚.

(2) Grazing incidence topography

By monochromatic X-ray we can get the grazing incidence topography, as shown below, and the diffraction vector is g = [11-24].

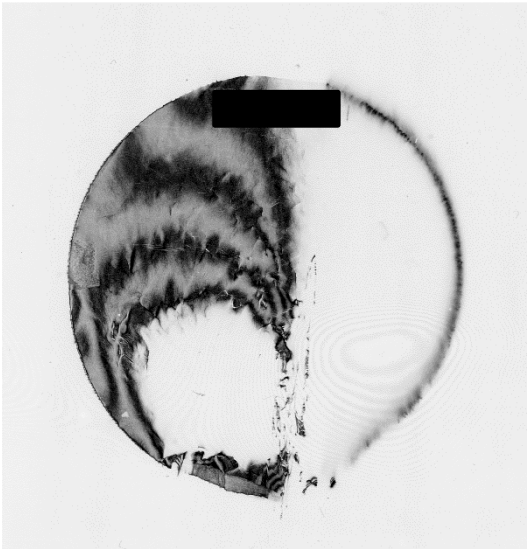

Figure 3.19 Grazing topography [11-24] showing TEDs and TSDs.

With 6 sets of contours only about half of the wafer is covered indicating relatively large curvature and high residual stresses. For the reason that this region contains large amount of residual stresses, this kind of residual stresses can affect the diffraction of the sample, then lots of distortions can be observed from the grazing incidence images. We select 3 different positions to calculate the threading dislocation density, the 3 positions are the same as the transmission part in Figure 3.3. And then we use the Nomarski Optical Microscopy to get the magnified images, as shown below:

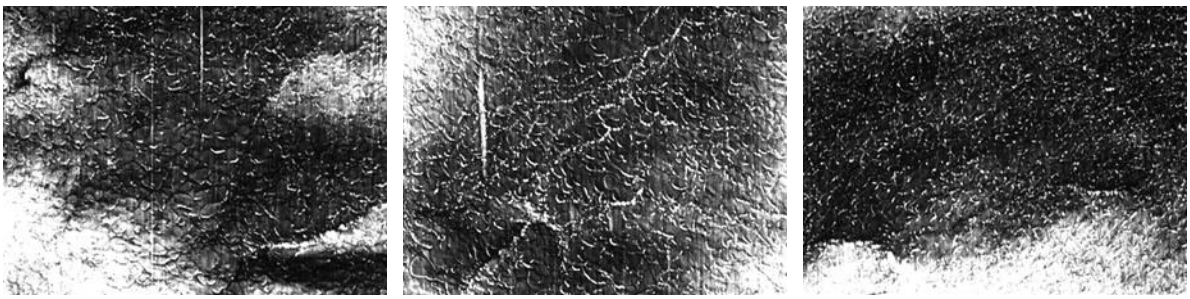

(1) (2) (3)

Figure 3.20 Magnified images of grazing incidence topographs for 3 positions of sample 3.

By counting the number of TDs of each area, we can get the threading dislocation density, as shown in Table 3.6.

Table 3.6 TDs density for 3 positions of sample 3

Position	1	2	3
TDs density ($\times 10^4 cm^{-2}$)	1.51	1.83	1.93

The average density is about $1.756\times10^4 cm^{-2}$. The density in the center (position 1) is relatively lower than that in other positions. The threading dislocations are formed during the growth of the crystal, so the factors such as operation, thermal gradient, growth environment, all that kind of factors during the growth can affect the property of the threading dislocations.

Sample 4—AlN-4

(1) Transmission topography

For this sample, characterization was carried out described in previous sections. The transmission images are shown below, and thickness for this sample, is 481 microns.

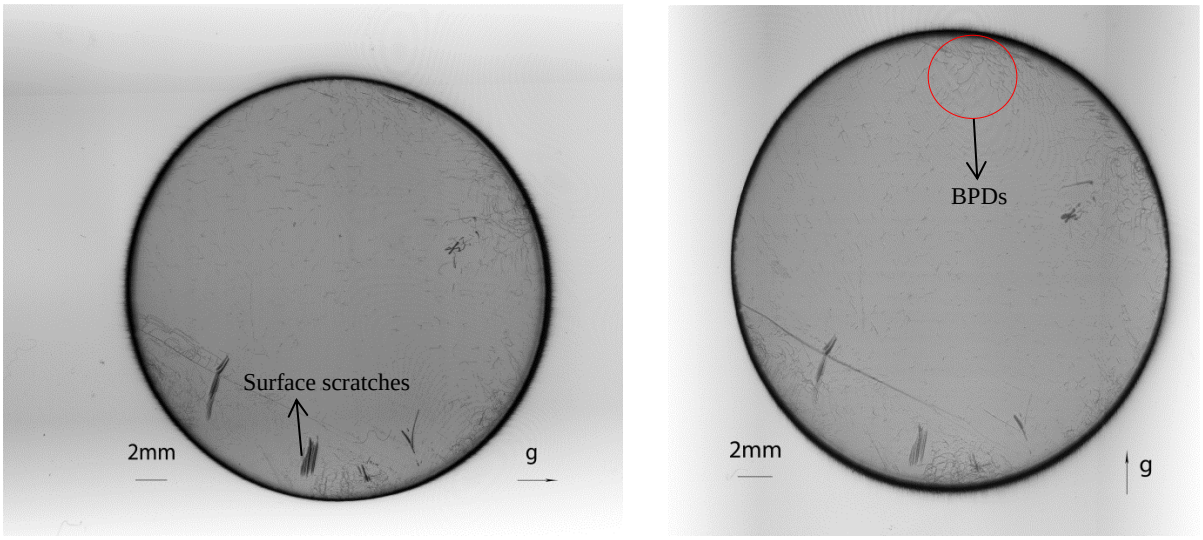

(a) (b)

Figure 3.21 Transmission topographs for (a) g = [11-20] and (b) g = [1-100] showing BPDs.

Also, we get the magnified images for 5 different positions as below from the microscope.

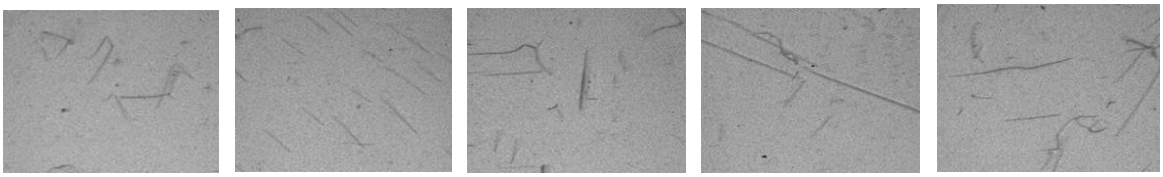

(1) (2) (3) (4) (5)

Figure 3.22 Magnified images of transmission topographs for 5 positions.

And then we can get the BPDs dislocation density for 5 different positions as the Table 3.7shown below:

Table 3.7 BPD density for 5 positions

Position	1	2	3	4	5
BPD density ($\times 10^4 cm^{-2}$)	0.071	0.048	0.033	0.017	0.069

Wafer is nearly dislocation-free with few basal plane dislocations (BPDs) and threading dislocations. It's clear to see the BPDs from the images, and wafer is nearly free of low angle grain boundaries (LAGBs). From the magnified images of the BPDs, it's clear to observe that these BPDs may be in many situations, for example, they may be parallel with each other, or just separate from each other. Also, we can observe some surface scratches, they may be formed during the processing and can be also observed by microscope.

(2) Grazing incidence topography

By monochromatic X-ray we can get the grazing incidence topography, as shown in Figure 3.23, and the diffraction vector is $\vec{g}$ = [11-24].

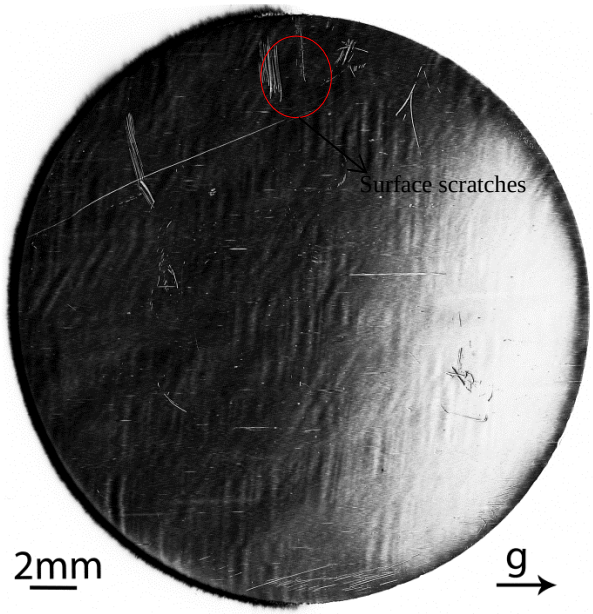

Figure 3.23 Grazing topograph [11-24] showing TEDs and TSDs.

And then we can get the BPDs dislocation density for 5 different positions as the Table 3.8 shown below:

Table 3.8 TDs density for 5 positions

Position	1	2	3	4	5
TED density ($\times 10^4 cm^{-2}$)	0.041	0.066	0.077	0.031	0.14
TSD density ($\times 10^4 cm^{-2}$)	0.020	0.005	0.010	<0.001	0.013

Most of the wafer is covered by about 2 sets of contour indicating small curvature in the wafer and low residual stresses. The threading dislocation density is relatively lower compared with other samples above. From the threading dislocation distribution we can see that, dislocation density of some regions around the edge is lower compared with that in the center of the wafer. The possible reason is that during the growth of crystal boule, the curvature radius is small around the edge. And the growth steps are larger around the edge compared with that in the center, in this way, the curvature radius will be steeper. As a result, it's difficult for threading dislocation to propagate in this kind of region. Therefore, the dislocation density is lower around the edge of the wafer than that in the center.

3.3.2 GaN

Sample 1—A (C-plane)

(1) Transmission topography

By white beam synchrotron X-ray topography, we can record transmission topographs as shown below (Figure 3.24). For this c-plane - (0001) wafer, and the 11-20 transmission image will reveal the distribution of BPDs. And we get the thickness of this sample by micrometer, is 313 microns. Similar to AlN wafer images, SPOT Application software is used to measure the total length of BPDs and estimate the dislocation density. For this sample, rather than selecting small areas, the entire wafer area was measured as the dislocation density is relatively low. Additionally, dislocations are only concentrated in one region of the sample as is shown in Figure 3.24, with a few dislocations near the edge of the sample.

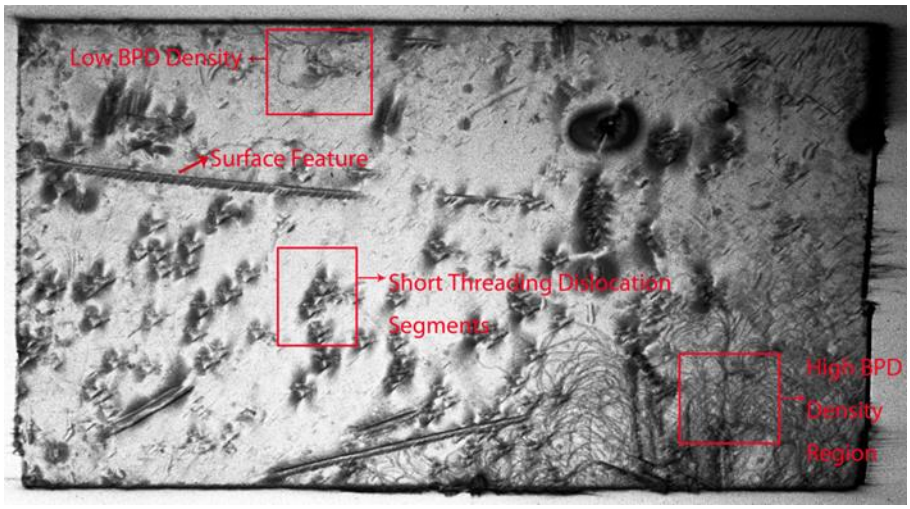

Figure 3.24 Transmission topograph of GaN c-plane wafer showing BPDs.

The whole area of this sample is 0.87 cm × 0.48 cm, total length of BPDs in this sample is 1963130 μm. Thus the BPD dislocation density is $1.509 \times 10^{4}cm^{-2}$. BPDs are non-uniformly distributed, with high BPD density region in the left side and low BPD density region around the top area. What's more, there are some short threading dislocation segments indicated in Figure 3.24. Basal plane dislocation (BPD) nucleated from the edges expand and propagate into the wafer. Most of regions of the wafer appear to be nearly BPD-free. Besides these dislocations, there are also some surface features which we can also observe using the microscope.

(2) Grazing incidence topography

By monochromatic beam synchrotron X-ray topography, we can get the grazing incidence topograph shown below (Figure 3.25). From the images, we can observe an array of threading dislocations. The dislocations with larger feature size are the threading screw dislocation (TSD). As indicated in the magnified image, the threading edge dislocation is shown below inset. In this case, we also can calculate the dislocation density in the entire wafer. The TED density is measured to be $0.5824\times10^{4}cm^{-2}$, and the TSD density is $0.08812\times10^{4}cm^{-2}$.

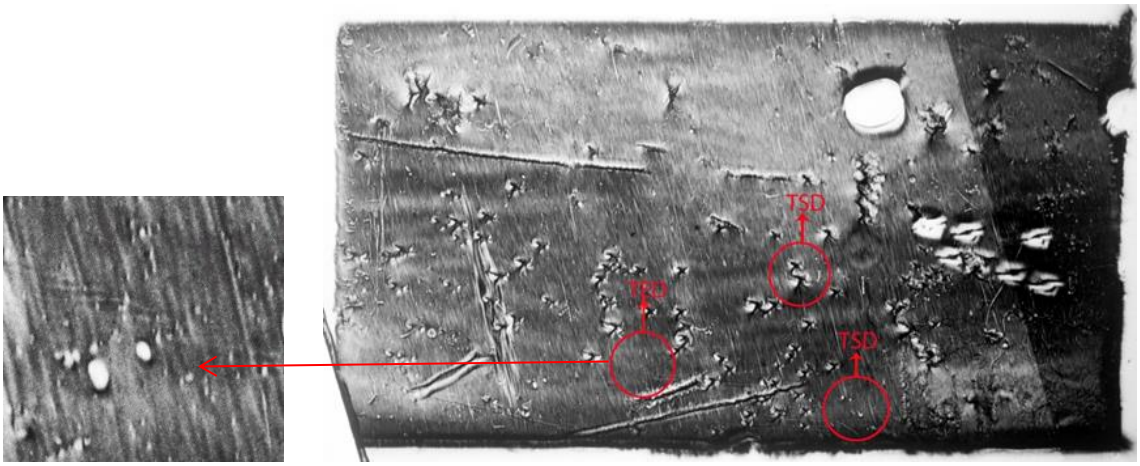

Figure 3.25 Grazing incidence topograph showing TSDs and TEDs.

Sample 2-- X6452-042-2 (C-plane)

(1) Transmission topography

By white beam synchrotron X-ray topography, we can get the transmission topographs shown below (Figure 3.26).

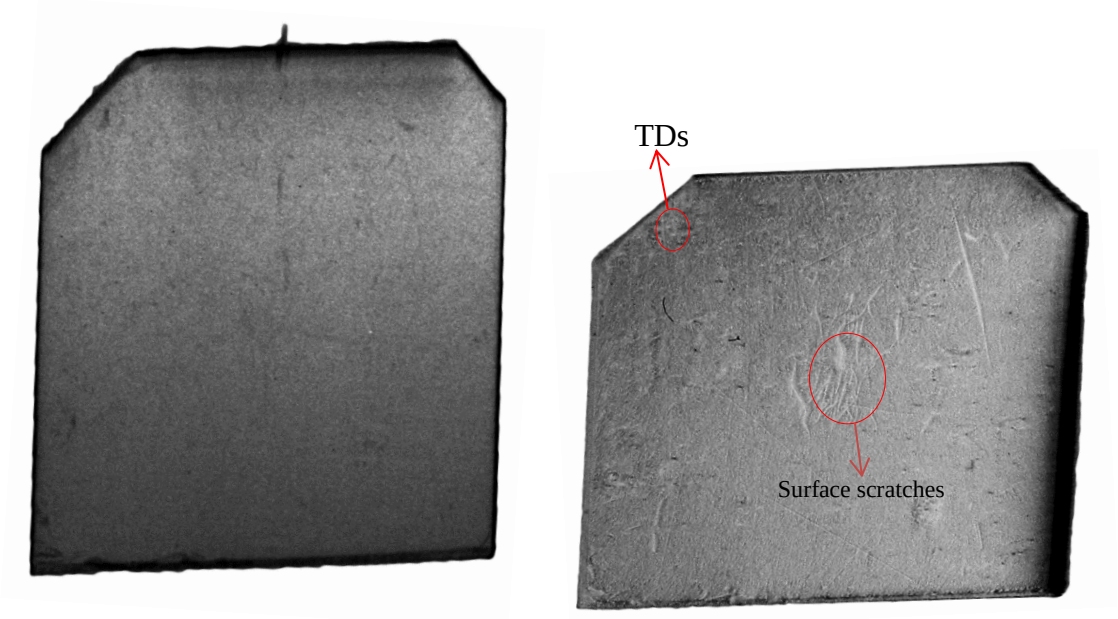

Figure 3.26 Transmission topographs of c-plane GaN wafer.

Contrast is strongly affected by numerous surface scratches, these scratches prevent resolution of defects. What's more, it is hard to observe BPDs from these transmission topographs, and it is likely to contain a high dislocation density. As a result, from these images, we can only observe some threading dislocations as indicated in the figure.

(2) Grazing incidence topography

By monochromatic beam synchrotron X-ray topography, we can get the grazing incidence topograph shown below (Figure 3.27). Most of the wafer is covered by 3 sets of contour indicating some threading dislocations. By SPOT Application software we can get the area covered by contour is about 0.6632 cm^2. The number of TSD in this area is 181, then we can get the TSD density for this sample is $2.729\times10^2 cm^{-2}$. In the same way, the number of TED in this area is 1302, and the TED density for this sample is $1.963\times10^3 cm^{-2}$.

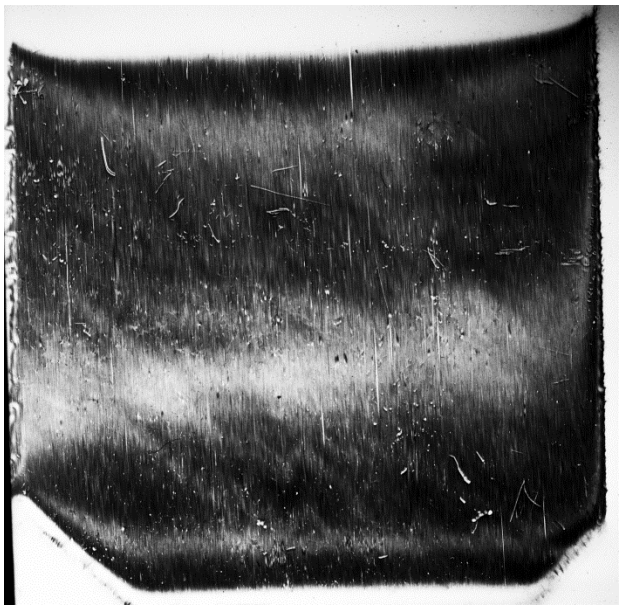

Figure 3.27 Grazing incidence topograph showing TSDs and TEDs.

Sample 3-- X2362-004-1 (C-plane)

(1) Transmission topography

By white beam synchrotron X-ray topography, we can get the transmission topographs shown below (Figure 3.28). It's hard to observe the BPDs, and contrast is strongly affected by numerous surface scratches. These scratches prevent resolution of defects.

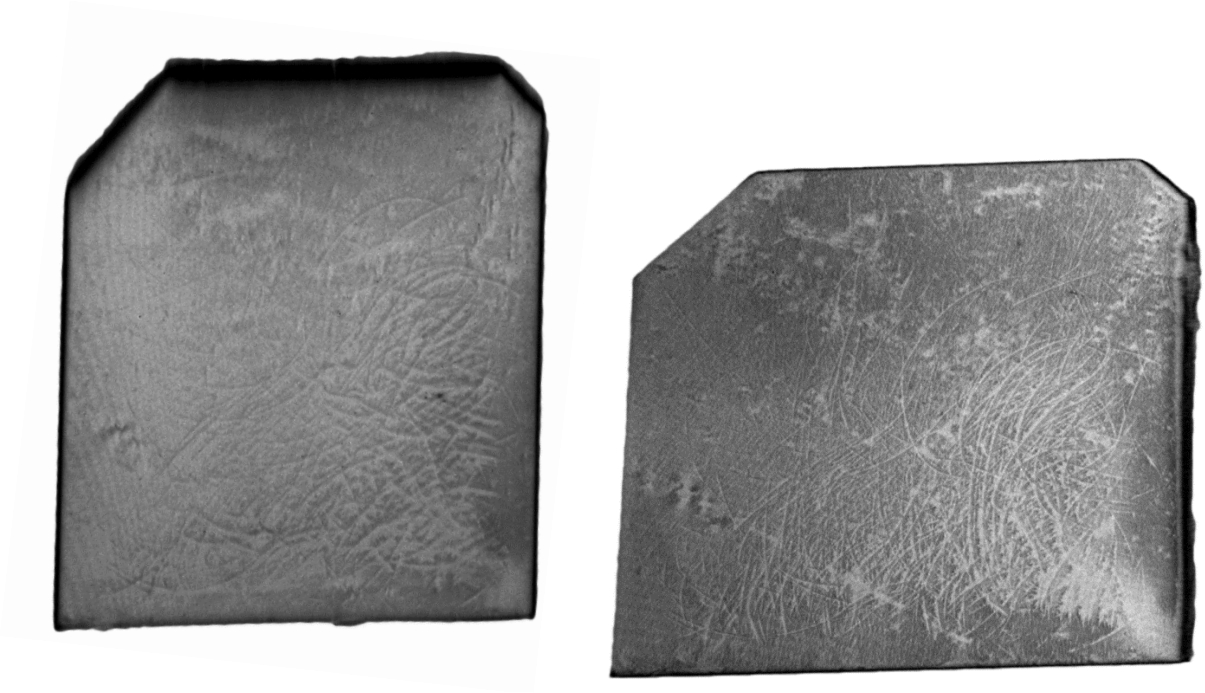

Figure 3.28 Transmission topographs of c-plane GaN wafer of 11-20 and 1-100.

(2) Grazing incidence topography

By monochromatic beam synchrotron X-ray topography, we can get the grazing incidence topograph shown below (Figure 3.29). Most of the wafer is covered by 2 sets of contour indicating some threading dislocations. By SPOT Application software we can get the area covered by contour is about 0.6265 cm^2. The number of TSD in this area is 246, then we can get the TSD density for this sample is $3.972\times10^2 cm^{-2}$. In the same way, the number of TED in this area is 1061, and then the TED density for this sample is $1.674\times10^3 cm^{-2}$.

Figure 3.29 Grazing incidence topograph showing TSDs and TEDs.

Sample 4-- Z5252-002-1 (A-plane)

(1) Transmission topography

By white beam synchrotron X-ray topography, we can get the transmission topography shown below (Figure 3.30). The scratches degrade the defects contrast strongly, and we can observe a group of deep scratches around the center of the sample. Besides these deep scratches, there are some fine scratches all around the wafer.

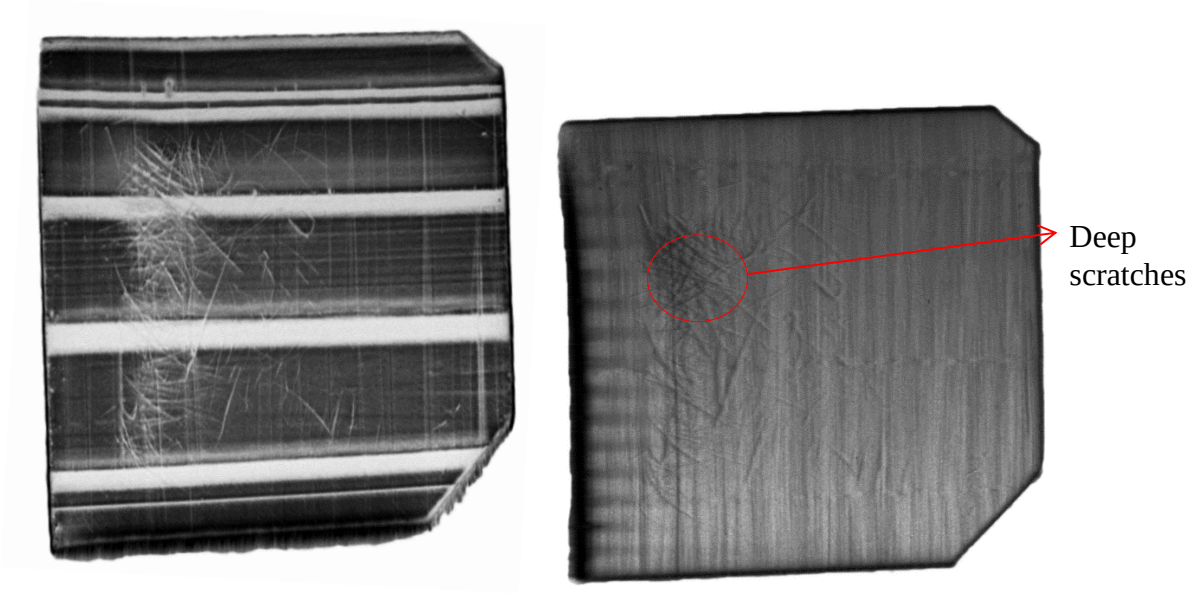

Figure 3.30 Transmission topographs of A-plane GaN wafer of 11-20 and 1-100.

Sample 5-- Y5252-002-1 (M-plane)

(1) Transmission topography

By white beam synchrotron X-ray topography, we can get the transmission topography shown below (Figure 3.31). There are a lot surface scratches on the wafer, in this way, the defects contrast will be degraded strongly.

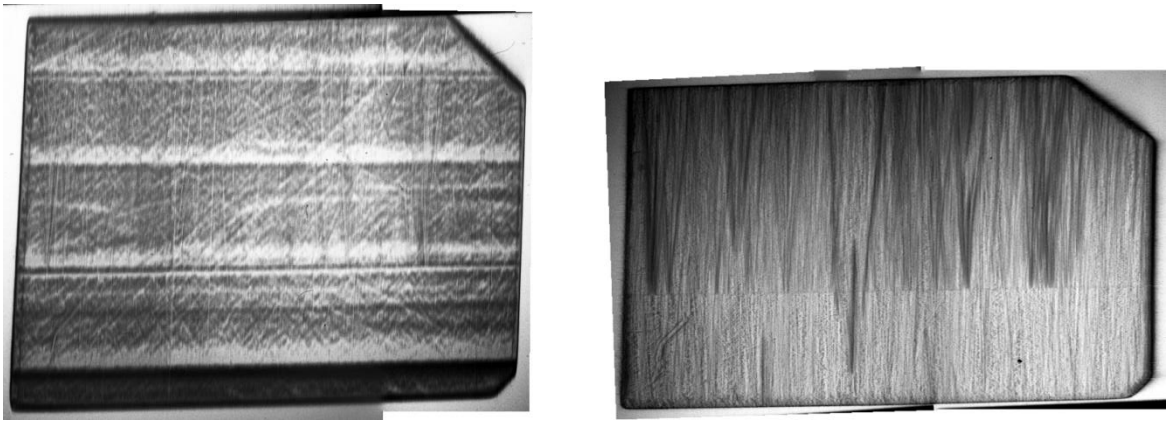

Figure 3.31 Transmission topographs of M-plane GaN wafer of 11-20 and 1-100.

(2) Grazing incidence topography

By monochromatic beam synchrotron X-ray topography, we can get the grazing incidence topography shown below (Figure 3.32). In this case, we record a small part of the wafer with 2 sets of contour. For this M-plane wafer, it's hard to observe threading dislocations from the grazing incidence images.

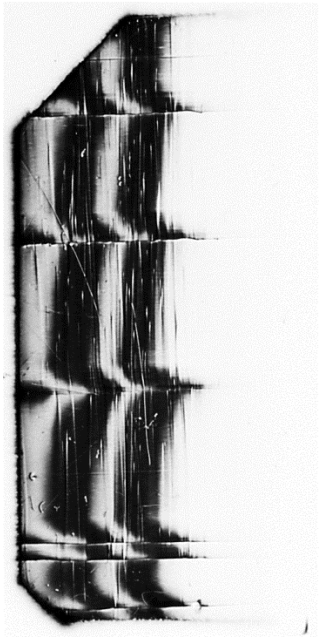

Figure 3.32 Grazing incidence topograph.

3.4 Conclusion

3.4.1 AlN

In this experiment, we conduct 4 AlN samples. In order to make a comparison among these samples, we can take a look at Table 3.9 and Table3.10.

Table 3.9 Dislocation counts (transmission topographs)

Position / Sample	1 (cm^{-2})×10^4	2 (cm^{-2})×10^4	3 (cm^{-2})×10^4	4 (cm^{-2})×10^4	5 (cm^{-2})×10^4	Average (cm^{-2})×10^4
AlN-1	0.357	2.430	1.980	2.360	0.608	1.5470
AlN-2	0.776	1.833	1.425	1.198	1.558	1.3580
AlN-3	1.632	1.405	1.389	>10	1.336	1.632
AlN-4	0.071	0.048	0.033	0.017	0.069	0.0476

Table 3.10 Dislocation counts (grazing incidence topographs)

Position / Sample	1 (cm^{-2})×10^4	2(cm^{-2})×10^4	3(cm^{-2})×10^4	4(cm^{-2})×10^4	5(cm^{-2})×10^4	Average (cm^{-2})×10^4
AlN-1	0.51	0.88	1.34	-	-	0.910
AlN-2	0.5575	1.5735	1.2988	4.477	4.125	2.4064
AlN-3	1.51	1.83	1.93	-	-	-
AlN-4	0.06	0.07	0.087	0.03	0.148	0.079

By the synchrotron X-ray topography, the defects of different wafers are observed. In usual, the dislocation density of the central part is lower than that around the edge. With the help of Nomarski Microscopy, we can get the magnified images in order to study some special areas, such as the hexagonal shape grain boundaries.

The main defects are BPDs, TSDs and TEDs but depending on the growth conditions employed during PVT growth, the density and distribution of each defect type in the wafers is different. Clearly, the control and optimal variations of growth parameters will play a determining role in the defect content and therefore, the applicability of these wafers in electronic and optoelectronics applications.

3.4.2 GaN

In this experiment, we conduct 5 GaN samples. In order to make a comparison among these samples, we can take a look at Table 3.11.

Table 3.11 Dislocation counts (transmission and grazing incidence topographs)

Dislocation / Sample	BPD (cm^{-2})×10^4	TED (cm^{-2})×10^4	TSD (cm^{-2})×10^4
A(C-plane)	1.509	0.5824	0.08812
X6452-042-2 (C-plane)	-	0.1963	0.02729
X2362-004-1 (C-plane)	-	0.1674	0.03927
Z5252-002-1 (A-plane)	-	-	-
Y5252-002-1 (M-plane)	-	-	-

In case of the c-plane wafers grown on ammonothermal substrates by HVPE method, defects densities are of the order of 10^4 cm^{-2}, which is more than 2 orders of magnitude lower than the highest quality HVPE wafers grown on sapphire substrates. Clearly, this approach for obtaining GaN wafers would be preferable for electronic and opto-electronic applications.

Chapter 4.Summary

4.1 Conclusion

In this study, the characterization of aluminum nitride (AlN) and gallium nitride (GaN) samples was carried out and defect distribution analyzed, with the help of a few techniques, such as synchrotron X-ray topography and Nomarski optical microscopy. For AlN samples, they show a wide range of densities from as low as $1.7\times10^{2}cm^{-2}$ to greater than $10^{6}cm^{-2}$. Usually, the dislocation distribution varies from wafer to wafer. In general, the BPDs are generated around the edge of the wafer, then propagating into the center of the wafer. TEDs and TSDs likely propagate from the seed but depending on the thermal gradients, TEDs could result from prismatic slip. For GaN wafers, the dislocation distribution can be totally different from wafer to wafer depending on orientation and growth process. The average BPDs density for c-plane sample is about $1.509\times10^{4}cm^{-2}$ and for TEDs, the dislocation density is of the order of a few $10^{3}cm^{-2}$, and TSD density is about $10^{2}cm^{-2}$. The BPDs distribution show very non-uniform, and they are concentrated in one region of the wafer. TEDs and TSDs density is relatively low.

To carry out analysis of X-ray topography and optical microscopy data, software such as, Laue Pt [23], SPOT Application and Photoshop have been employed during the analysis. The basal plane dislocation density, threading edge dislocation density, and threading screw dislocation density are measured. Other defects, like low angle grain boundaries and prismatic slip bands are also observed. There are some surface features that can be observed by microscopy, such as the surface scratches, and they can degrade the defects contrast strongly.

4.2 Further Work

For aluminum nitride samples, high resolution X-ray diffraction (HRXRD) experiments can be carried to obtain quantitative information on crystalline quality of the wafers. As for the gallium nitride samples, more studies on the A-plane and M-plane can be conducted by synchrotron X-ray topography in different geometries.

Reference

[1] Orton, J. W., & Foxon, C. T. 1998. Group III nitride semiconductors for short wavelength light-emitting devices. Reports on Progress in Physics, 61(1): 1–75.

[2] Kneissl, M., Kolbe, T., Chua, C., Kueller, V., Lobo, N., et al. 2010. Advances in group III-nitride-based deep UV light-emitting diode technology. Semiconductor Science and Technology, 26(1): 014036.

[3] Walukiewicz1, W., Ager, J. W., Yu, K. M., & Weber, Z. L. 2006, February 17. Structure and electronic properties of InN and In-rich group III-nitride alloys. JOURNAL OF PHYSICS D: APPLIED PHYSICS.

[4] Kwong, F., Li, L., Ann, S., & Hass, Z. 2011. Gallium Nitride: An Overview of Structural Defects. Optoelectronics - Materials and Techniques.

[5] Sintonen, S., Rudziński, M., Suihkonen, S., Jussila, H., Knetzger, M., et al. 2014. Synchrotron radiation X-ray topography and defect selective etching analysis of threading dislocations in GaN. Journal of Applied Physics, 116(8): 083504.

[6] Cheng, Y. C., Wu, X. L., Zhu, J., Xu, L. L., Li, S. H., et al. 2008. Optical properties of rocksalt and zinc blende AlN phases: First-principles calculations. Journal of Applied Physics, 103(7): 073707.

[7] Speck, J., & Rosner, S. 1999. The role of threading dislocations in the physical properties of GaN and its alloys. Physica B: Condensed Matter, 273-274: 24–32.

[8] Raghothamachar, B., Vetter, W. M., Dudley, M., Dalmau, R., Schlesser, R., et al. 2002. Synchrotron white beam topography characterization of physical vapor transport grown AlN and ammonothermal GaN. Journal of Crystal Growth, 246(3-4): 271–280.

[9] Raghothamachar, B. 2001. Synchrotron white beam X-ray characterization of growth defects in bulk compound semiconductors. thesis.

[10] Rojo, J. C., Slack, G. A., Morgan, K., Raghothamachar, B., Dudley, M., et al. 2001. Report on the growth of bulk aluminum nitride and subsequent substrate preparation. Journal of Crystal Growth, 231(3): 317–321.

[11] Watson, I. M. 2013. Metal organic vapour phase epitaxy of AlN, GaN, InN and their alloys: A key chemical technology for advanced device applications. Coordination Chemistry Reviews, 257(13-14): 2120–2141.

[12] Hartmann, C., Dittmar, A., Wollweber, J., & Bickermann, M. 2014. Bulk AlN growth by physical vapour transport. Semiconductor Science and Technology, 29(8): 084002.

[13] Zhuang, D., Herro, Z., Schlesser, R., Sitar, Z., 2006. Journal of Crystal Growth 287, 372–375.

[14] Yano, M., Okamoto, M., Yap, Y., Yoshimura, M., Mori, Y., et al. 2000. Growth of nitride crystals, BN, AlN and GaN by using a Na flux. Diamond and Related Materials, 9(3-6): 512–515.

[15] Patent US7063741 - High pressure high temperature growth of crystalline group III metal nitrides, Google Patents. (n.d.). http://www.google.com/patents/US7063741 (accessed April 20, 2017).

[16] Tian, Y., Shao, Y., Wu, Y., Hao, X., Zhang, L., et al. 2015. Direct growth of freestanding GaN on C-face SiC by HVPE. Scientific Reports, 5: 10748.

[17] Sintonen, S., Rudziński, M., Suihkonen, S., Jussila, H., Knetzger, M., et al. 2014. Synchrotron radiation X-ray topography and defect selective etching analysis of threading dislocations in GaN. Journal of Applied Physics, 116(8): 083504.

[18] Raghothamachar, B., Dhanaraj, G., Bai, J., & Dudley, M. 2006. Defect analysis in crystals using X-ray topography. Microscopy Research and Technique, 69(5): 343–358.

[19] Sintonen, S. 2014. Synchrotron radiation X-ray topography of crystallographic defects in GaN. thesis, Aalto University publication series, Unigrafia Oy Helsinki .

[20] Dudley, M. Structure of Materials Lecture Notes: 1-2.

[21] Lowney, D., Perova, T. S., Nolan, M., Mcnally, P. J., Moore, R. A., et al. 2002. Investigation of strain induced effects in silicon wafers due to proximity rapid thermal processing using micro-Raman spectroscopy and synchrotron X-ray topography. Semiconductor Science and Technology, 17(10): 1081–1089.

[22] Zhou, T., Raghothamachar, B., Wu, F., Dalmau, R., Moody, B., et al. 2014. Characterization of Threading Dislocations in PVT-Grown AlN Substrates via X-Ray Topography and Ray Tracing Simulation. Journal of Electronic Materials, 43(4): 838–842.

[23] Huang, X. R. 2010. LauePt, a graphical-user-interface program for simulating and analyzing white-beam X-ray diffraction Laue patterns. Journal of Applied Crystallography, 43(4): 926–928.